Accepted Manuscript

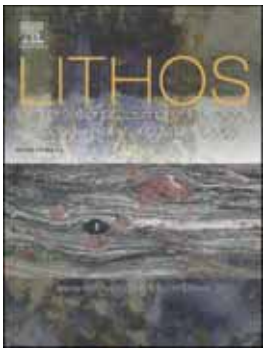

New constraints on the cretaceous geodynamics of paleo-Pacific plate subduction: Insights from the Xiaojiang–Beizhang granitoids, Zhejiang Province, Southeast China

Liang Liu, Rui-Zhong Hu, Hong Zhong, Yan-Wen Tang, Jie-Hua Yang, Zhen Li, Jiao-Long Zhao, Neng-Ping Shen

PII: S0024-4937(18)30222-6
DOI: doi:10.1016/j.lithos.2018.06.020
Reference: LITHOS 4696

To appear in: *LITHOS*

Received date: 5 May 2018
Accepted date: 20 June 2018

Please cite this article as: Liang Liu, Rui-Zhong Hu, Hong Zhong, Yan-Wen Tang, Jie-Hua Yang, Zhen Li, Jiao-Long Zhao, Neng-Ping Shen , New constraints on the cretaceous geodynamics of paleo-Pacific plate subduction: Insights from the Xiaojiang–Beizhang granitoids, Zhejiang Province, Southeast China. Lithos (2018), doi:10.1016/j.lithos.2018.06.020

New constraints on the Cretaceous geodynamics of paleo-Pacific plate subduction: insights from the Xiaojiang–Beizhang granitoids, Zhejiang Province, southeast China

Liang Liu[a,*] liuliang@vip.gyig.ac.cn, Rui-Zhong Hu[a,b], Hong Zhong[a,b], Yan-Wen Tang[a], Jie-Hua Yang[a,b], Zhen Li[c], Jiao-Long Zhao[d] and Neng-Ping Shen[a,b]

[a]State Key Laboratory of Ore Deposit Geochemistry, Institute of Geochemistry, Chinese Academy of Sciences, Guiyang 550081, China

[b]College of Earth Sciences, University of Chinese Academy of Sciences, Beijing 100049, China

[c]John de Laeter Centre, Faculty of Science and Engineering, Curtin University, GPO Box U1987, Perth, WA 6845, Australia

[d]School of Earth Sciences, Gansu Key Laboratory of Mineral Resources in Western China, Lanzhou University, Lanzhou 730000, China

[*]**Corresponding author.**

ABSTRACT

The relationship between the evolution of Cretaceous magmatism along the southeastern margin of Eurasia and subduction of the paleo-Pacific plate remains controversial. Here we investigate the petrogenesis of the Xiaojiang–Beizhang ferroan and magnesian granitoids, melanocratic microgranular enclaves (MME) that are found within the granitoids, and an associated mafic dyke exposed in southeast China to

provide new constraints on the geodynamics of paleo-Pacific plate subduction. Zircon U–Pb ages indicate that the ferroan and magnesian granitoids were emplaced in the Cretaceous (ca. 120 and 110 Ma, respectively), and that the MME and mafic dyke are coeval with their host granitoids. Geochemical characteristics imply that the granitoids were produced by partial melting of crustal rocks and mixed with mantle-derived magmas. The MME are derivatives of the mafic magmas that intruded the silicic magmas. Two phases of mafic magmatism are evident. Stage 1 mafic rocks (the ca. 120 Ma MME) were derived mainly from the subcontinental lithospheric mantle (SCLM) with some contribution from asthenospheric mantle. The parental mafic magmas for Stage 2 (the ca. 110 Ma MME and mafic dykes) were derived from interaction and metasomatism of the SCLM and asthenosphere with slab-derived fluids. Iron enrichment or depletion in the granitoids was controlled mainly by oxygen fugacity and pressure. Our new data, combined with previously published data from Cretaceous igneous rocks in southeastern China, reveal major geochemical changes at 136 and 118 Ma, respectively. The 132–119 Ma igneous rocks record the minimal addition of slab-derived components to their source, and provide strong evidence for an abrupt change in the direction of motion of the paleo-Pacific plate from southwest to northwest at ca. 125–122 Ma.

Keywords: Ferroan and magnesian granitoids; Mafic microgranular enclaves; Magma mixing/mingling; paleo-Pacific plate; subduction; southeast China

1. Introduction

Coupling between the subducting plate and overlying continental lithosphere plays a key role in plate tectonics, although geological records indicating long-term coupling are generally not well preserved (Sun et al., 2007). Late Mesozoic igneous rocks associated with economically significant Au, Ag, Cu, Mo, Zn, Pb, W, Sn, Sb and U mineral deposits are widespread in southeastern China (Zhou et al., 2006). The rocks are dominated by granitoids and equivalent volcanic rocks (Fig. 1) that can be divided into two age groups: Jurassic (196–140 Ma; referred to as Early Yanshanian) and Cretaceous (140–86 Ma; Late Yanshanian) (Li et al., 2007; Zhou and Li, 2000). The Cretaceous rocks are generally found along the coast, and are widely accepted to be related to subduction of the paleo-Pacific plate (Fig. 1) (He and Xu, 2012; Li et al., 2014a, b; Li and Li, 2007; Liu et al., 2016b; Zhou et al., 2006). Study of these rocks provides an opportunity to evaluate the effects of subduction on the evolution of the overlying crust. Nevertheless, how the evolution of Cretaceous magmatism relates to the processes of subduction of the paleo-Pacific plate remain controversial (Li et al., 2014a, b; Li and Li, 2007; Liu et al., 2016b; Sun et al., 2007; Zhou et al., 2006).

A number of paleo-Pacific subduction models have been proposed to explain Cretaceous magmatism in southeastern China. For example, Zhou and Li (2000) suggested that the dip of the subducting Pacific slab increased from a very low angle to a moderate angle during the period from 180 to 80 Ma, resulting in an oceanward migration of magmatic activity (i.e., towards the southeast). This model is disputed

based on the distribution of late Mesozoic magmatic rocks in southeastern China (Li and Li, 2007). Alternatively, a flat-slab subduction and slab-foundering model was proposed by Li and Li (2007) to account both for the large width of the Indosinian orogen and broad Mesozoic magmatic province. Subsequently, Li et al. (2007) suggested a slab break-off and rollback mechanism to explain the distribution of Jurassic igneous rocks in southeastern China. Based on the study of some Cretaceous syenitic and gabbroic rocks, He and Xu (2012) proposed that subduction of the paleo-Pacific plate beneath southeastern China evolved from slab advance to slab rollback at ca. 110 Ma, resulting in a transition from a compressional (141–118 Ma) to an extensional (98–86 Ma) tectonic regime. In a refinement of the slab breakoff and rollback model, Li et al. (2014b) proposed that, following slab rollback at 180–155 Ma, a recurrence of slab breakoff at ca. 125–115 Ma was followed by renewed slab rollback at ca. 115–90 Ma. Jiang et al. (2015) also favoured a slab advance and retreat model for the late Mesozoic tectonomagmatic evolution of southeastern China, considering that the belts of Early and Late Cretaceous A-type granite were the result of progressive slab rollback. More recently, Liu et al. (2016b) focussed on the contemporary volcanic sequences in the Zhejiang–Fujian provinces, and proposed northwestward subduction with increasingly asymmetric slab rollback after ca. 150 Ma. Importantly, contrasting directions of motion of subduction have been proposed for the paleo-Pacific plate in the Cretaceous. These include suggestions that the slab moved towards the northwest (Li et al., 2014a; Li and Li, 2007; Liu et al., 2016b;

Zhou and Li, 2000), or first towards the southwest followed by movement towards the northwest at ca. 125–122 Ma (Sun et al., 2007; Wang et al., 2011).

The mechanisms of crust–mantle interaction and the nature of the magmatic sources during the Cretaceous are poorly constrained, in particular regarding the role of the mantle in the formation of the Cretaceous granites. Melanocratic microgranular enclaves (MME) and/or mafic dykes are common in the Cretaceous granitoids of southeastern China (Griffin et al., 2002; Hsieh et al., 2009; Liu et al., 2013, 2016a; Wong et al., 2011). These mafic components provide an opportunity to investigate the petrogenesis of the granitoid magmas, and permit constraints on the role of the mantle and geodynamic setting in which the mafic rocks formed (Griffin et al., 2002;; Yang et al., 2007).

In this paper, we present data from Cretaceous ferroan and magnesian granitoids from the Xiaojiang–Beizhang areas, Zhejiang Province, which contain abundant fresh MME and/or mafic dykes. Using a detailed characterisation of the mineralogy, petrology, geochronology and geochemistry, including the Sr–Nd–Hf isotopic systematics, of the granitoids, MME and mafic dykes, we provide constraints on the origin of the Cretaceous granitoids and propose a general mechanism for iron depletion or enrichment in intermediate to silicic magmas (Zhu et al., 2016). Finally, our new data, when combined with previously published data for the Cretaceous igneous rocks, reveal fundamental geochemical changes at 136 and 118 Ma. The 132–119 Ma igneous rocks in southeastern China record limited addition of slab-derived

components to their magmatic sources, and provide evidence that the direction of motion of the paleo-Pacific plate broadly changed from southwest to northwest at ca. 125–122 Ma.

2. Geological background

The South China Block (SCB), composed of the Yangtze Block to the northwest and Cathaysia Block to the southeast, is one of the largest fragments of Precambrian crust in southeastern Eurasia (Fig. 2b). The two blocks are separated by the Jiangshan–Shaoxing Fault in the eastern SCB, although the relationship with the bounding rocks to the southwest is controversial. The timing of the amalgamation of the Yangtze and Cathaysia blocks was probably the early Neoproterozoic. Subsequently, the SCB collided with the Indochina Block (to the southwest) and the North China Block (to the north) in the Triassic (Zheng et al., 2013).

The basement of the Yangtze Block comprises mainly metamorphosed Proterozoic rocks and minor Archaean rocks (e.g., the Kongling Complex). In contrast, the basement to the Cathaysia Block consists predominantly of Neoproterozoic rocks with minor Palaeoproterozoic–Mesoproterozoic metamorphic rocks (Zheng et al., 2013 and references therein). Three major tectonothermal events took place in the SCB during the early to middle Palaeozoic, Triassic and Jurassic–Cretaceous, which are traditionally termed the Caledonian, Indosinian and Yanshanian events, respectively. The Jurassic–Cretaceous granitoids and volcanic rocks of the SCB are mainly concentrated within the southeast region. Of these, Jurassic granitoids are

concentrated in the inland region, whereas the Cretaceous granitoids and silicic volcanic rocks are mainly distributed in the coastal region (Zhou et al., 2006).

3. Field relations and petrography

The Xiaojiang pluton is located in the Cathaysia Block and crops out in the eastern part of Xinchang County, Zhejiang Province. The pluton intrudes Lower Cretaceous volcanic rocks of the Moshishan Group, and has an outcrop area of ~150 km^2 (Fig. 2c). The main body is composed of quartz diorite and alkali feldspar granite, and in places the alkali feldspar granite is intruded by quartz diorite (Fig. 3a). The alkali feldspar granites are medium-grained, and consist of quartz (20–40 vol.%), alkali feldspar (45–60 vol.%), plagioclase (10–15 vol.%) and biotite (3–4 vol.%) (Fig. 4a), with accessory Fe–Ti oxides, zircon and apatite. Alkali feldspar occurs both as perthite and microcline. Biotite forms anhedral grains that are interstitial to feldspar (Fig. 4a). The ages of the alkali feldspar granites have been constrained by zircon U–Pb dating, and range from 113.5 ± 1.1 to 121.1 ± 0.9 Ma (Hsieh et al., 2009; Wang et al., 2013). The quartz diorites are medium- to fine-grained and consist of quartz (8–15 vol.%), alkali feldspar (20–25 vol.%), plagioclase (40–63 vol.%), biotite (10–14 vol.%), pyroxene (clinopyroxene and orthopyroxene; 3–6 vol.%), hornblende (2–5 vol.%) and Fe–Ti oxides (1–2 vol.%), with accessory zircon, titanite and apatite (Fig. 4b). Biotite occurs as bladed or euhedral tabular crystals. U–Pb zircon ages of 109.6 ± 0.9 and 114.3 ± 1.2 Ma have been obtained from the quartz diorites (Hsieh et al., 2009; Wong et al., 2011).

The Beizhang pluton is located ~6–7 km northwest of the Xiaojiang pluton. This pluton intrudes volcanic rocks of the Guantou and Moshishan groups, and has a total exposed area of ca. 42 km^2 (Fig. 2c). The Beizhang pluton is dominated by medium- to coarse-grained monzogranites, which consist of quartz (25–30 vol.%), alkali feldspar (21–25 vol.%), plagioclase (35–40 vol.%), biotite (6–8 vol.%), hornblende (1–3 vol.%) and Fe–Ti oxides (1–2 vol.%), with accessory titanite, zircon and apatite (Fig. 4c). Biotite occurs as euhedral tabular crystals.

Randomly distributed MME are ubiquitous and abundant within all lithologies. Those within the alkali feldspar granite range in size from 20 cm to >1 m in diameter, whereas those in the quartz diorite and monzogranite mostly range from several cm to 0.5 m across (Fig. 3b–e). Relative to their host rocks, most MME show well-rounded to elongate shapes, and are notably fine-grained (0.1–2 mm) and dark-coloured. The contacts between the MME and their host rocks are irregular or diffuse (Fig. 3b–e). Some MME show gulfs and embayments at their margins and enclose host rock xenocrysts, in particular of feldspar (Fig. 3d–e). In addition, mafic dykes with a thickness of several decimetres intrude the monzogranite within the Beizhang pluton (Fig. 3f).

MME within alkali feldspar granite lack amphibole and comprise plagioclase (30–40 vol.%), alkali feldspar (25–35 vol.%), quartz (15–20 vol.%) and biotite (8–10 vol.%). Accessory minerals are zircon, titanite, apatite and Fe–Ti oxides. Biotite grains are anhedral to acicular and interstitial to feldspar (Fig. 4d). Reported zircon

U–Pb ages for the MME are 103.2 ± 0.9 and 117.6 ± 1.0 Ma (Hsieh et al., 2009; Wang et al., 2013). The MME within the quartz diorite are composed of plagioclase (50–65 vol.%), alkali feldspar (15–20 vol.%), quartz (6–9 vol.%), biotite (12–16 vol.%), pyroxene (5–7 vol.%) and hornblende (3–5 vol.%), with accessory zircon, titanite, apatite and magnetite. Biotite varies from euhedral tabular crystals to subhedral bladed grains (Fig. 4e–f). The MME within the monzogranite consist of plagioclase (30–60 vol.%), alkali feldspar (15–30 vol.%), quartz (6–8 vol.%), biotite (10–17 vol.%), pyroxene (3–5 vol.%) and hornblende (1–4 vol.%), with accessory zircon, titanite, apatite and magnetite (Fig. 4g). Apatite within all MME occurs as euhedral acicular grains (Fig. 4f–g), consistent with quenching of the mafic magmas. Rocks from the mafic dykes are mainly dolerite, and show fine-grained (0.1–1 mm) and ophitic textures (Fig. 4h). They are composed of plagioclase (50–65 vol.%), clinopyroxene (25–30 vol.%) and orthopyroxene (5–11 vol.%), with minor olivine (0–5 vol.%) and magnetite (3 vol.%) (Fig. 4h).

Overall, the uncertainties associated with existing U–Pb zircon ages for individual samples are 4.3%–14.0%, and therefore, at least some of the ages should be incorrect. No isotopic dating has so far been undertaken on many of the lithologies (i.e., the monzogranite, MME within the quartz diorite and monzogranite and mafic dyke). In addition, previous studies using whole-rock geochemical and Sr–Nd isotopic data proposed that the Xiaojiang alkali feldspar granite, quartz diorite and MME were formed by mixing/minging of basaltic and granitoid magmas (Hsieh et al., 2009;

Wang et al., 2013). However, the large ambiguities in the results of whole-rock analyses have to be considered. Whole-rock analytical data provide just a snap-shot of the end result (Griffin et al., 2002), and only record the geochemical signatures of melts that have undergone magma mixing (Liu et al., 2016a).

4. Analytical methods

4.1. Zircon U–Pb dating, trace element and Lu–Hf isotope geochemistry

Zircon grains from seven samples were separated by standard density and magnetic techniques, and then selected by hand picking under a binocular microscope. Representative zircon grains were mounted in epoxy resin then polished to expose grain centres. The external morphology and internal structure of grains were characterised using transmitted and reflected light microscopy and cathodoluminescence (CL) images to guide the selection of analytical spots. CL images were acquired using a Mono CL4 detector (Gatan, U.S.A) attached to a JEOL JSM-7800F field emission scanning electron microscope at the State Key Laboratory of Ore Deposit Geochemistry (SKLODG), Institute of Geochemistry, Chinese Academy of Sciences (IGCAS), Guiyang, China. Operating conditions used an accelerating voltage of 10.0 kV and a primary beam current of 10 nA.

Zircon U–Pb dating and trace element analyses were performed simultaneously by LA-ICP-MS using a GeoLas Pro 193 nm ArF excimer laser at the SKLODG, IGCAS. Ion signal intensities were acquired using an Agilent 7900 ICP-MS instrument. Helium was used as a carrier gas and was mixed with argon via a

T-connector before entering the ICP-MS. Each analysis included a background acquisition (gas blank; ca. 18 s) before data acquisition (ca. 50 s). During analysis, the laser beam diameter, repetition rate and energy were 32 μm, 5 Hz and 8.0 J/cm^2, respectively. The U–Pb isotopic and trace element data were processed using the ICPMSDataCal software (Liu et al., 2010). Zircon 91500 was used as an external standard, whereas other reference materials (NIST 610, BHVO-2G, BCR-2G and BIR-1G) were used for calibrating the trace element data. The recommended trace element values for these standards were taken from the GeoReM database (http://georem.mpch-mainz.gwdg.de/). The Isoplot 4.15 software was used for weighted-mean calculations and for plotting concordia diagrams.

A Nu Plasma II MC-ICP-MS (Nu Instruments, Wrexham, Wales, UK) coupled to an Analyte Excite laser ablation system (Teledyne Cetac Technologies, Bozeman, Montana, USA) was used for *in situ* zircon Lu–Hf isotopic analyses at Nanjing FocuMS Technology Co. Ltd. Analyses were performed on spots immediately adjacent to spots already analysed for U–Pb age determinations. The laser beam diameter, repetition rate and energy were 50 μm, 8 Hz and 6.0 J/cm^2, respectively. Helium was used as a carrier gas, and zircon standards Mud Tank, GJ-1, 91500, Plešovice and Penglai were used for calibration. A $^{179}Hf/^{177}Hf$ ratio of 0.7325 was assumed as the normalising factor to correct for mass fractionation of Hf during analysis. In this study, measurements of zircon standards Mud Tank, GJ-1, 91500, Plešovice and Penglai gave $^{176}Hf/^{177}Hf$ ratios of 0.282518 ± 0.000006 (n = 16, 2σ),

0.282010 ± 0.000005 (n = 33, 2σ), 0.282306 ± 0.000008 (n = 19, 2σ), 0.282479 ± 0.000005 (n = 18, 2σ) and 0.282908 ± 0.000008 (n = 16, 2σ), respectively, all of which are consistent with recommended values within 2σ errors (Griffin et al., 2007).

4.2. Whole-rock and Sr–Nd isotope geochemistry

Selected fresh whole-rock samples were crushed and ground to 200 mesh in an agate ring mill for whole-rock geochemical analyses. Major element analysis was performed using a PANalytical PW2424 X-ray fluorescence (XRF) spectrometer at the ALS Chemex (Guangzhou) Co. Ltd, China. Mixtures of whole-rock powders (~0.9 g) and lithium borate flux (50%–50% $Li_2B_4O_7$–$LiBO_2$) were fused into glass discs and then analysed by XRF. Loss on ignition (LOI) values were determined by heating 1 g of powder to 1000°C for 1 h. The analytical precision is generally better than 5%. Trace elements were measured using a Perkin-Elmer Sciex ELAN DRC-e Q-ICP-MS at SKLODG, IGCAS. Whole-rock powders (50 mg) were dissolved in PTFE-lined stainless steel bombs using a HF + HNO_3 mixture for 48 h at ~190°C. An internal Rh standard was used to monitor signal drift during counting. The international standards GBPG-1, AGV-2 and AMH-1 were used for monitoring data quality. The analytical precision is estimated to be better than 10%; detailed analytical procedures are described in Qi et al. (2000).

Whole-rock Sr–Nd isotopic analyses were undertaken using a Nu Plasma HR MC-ICP-MS in the Radiogenic Isotope Facility at the University of Queensland, Australia. Analyses used ca. 100 mg of dissolved bulk rock powder. Normalisation to

$^{86}Sr/^{88}Sr$ = 0.1194 and $^{146}Nd/^{144}Nd$ = 0.7219 were employed for mass fractionation corrections. Nd isotopic drift was monitored using an in-house Nd standard (Ames Nd Metal). During analysis, the measured $^{87}Sr/^{86}Sr$ ratio for NBS-987 and the $^{143}Nd/^{144}Nd$ ratio for Nd Metal were 0.710249 ± 4 (n = 12, 2σ) and 0.511965 ± 2 (n = 15, 2σ), respectively, which are consistent with the long-term values (0.710249 ± 28 and 0.511966 ± 16, respectively) measured by TIMS. Measurements of reference materials BCR-2 and BHVO-2 gave $^{87}Sr/^{86}Sr$ = 0.705021 ± 0.000008 and 0.703476 ± 0.000007 and $^{143}Nd/^{144}Nd$ = 0.512629 ± 0.000003 and 0.512983 ± 0.000004, respectively, which are identical to the reported reference values from the GeoReM database.

4.3 Mineral chemistry

Mineral chemical analyses were carried out using an EPMA-1600 electron probe microanalyser at the SKLODG, IGCAS, using natural minerals for standards. During analysis, the accelerating voltage, specimen current and beam diameter were 25 kV, 10 nA and 1μm, respectively.

5. Results

5.1. Zircon U–Pb dating and trace element compositions

Seven samples (XJ-2, XJ-4, XJ-5, XJ-10, XJ-13, BZ-1 and BZ-5), including five from the Xiaojiang pluton and two from the Beizhang pluton, were selected for zircon U–Pb dating and trace element analysis. CL images of representative zircon grains are shown in Fig. 5. The results of zircon U–Pb dating and trace element analysis are

listed in Supplementary Tables S1 and S2, and presented graphically in Fig. 6. Uncertainties are quoted at 2σ for the weighted mean ages.

5.1.1. Zircon U–Pb dating

All zircon crystals from the Xiaojiang and Beizhang plutons are prismatic, euhedral to subhedral and colourless to pale yellow. Grains have a length of 70–220 μm and aspect ratios of 1:1 to 3:1. In CL images, grains show magmatic oscillatory zoning or occasional typical zoning absorption (Fig. 5), and most have relatively high Th/U ratios (Supplementary Table S1) indicative of a magmatic origin. No inherited cores were observed.

All 14 zircon analyses from sample XJ-10 (alkali feldspar granite) are concordant and yield a weighted-mean $^{206}Pb/^{238}U$ age of 120.0 ± 0.9 Ma (MSWD = 0.61; 2σ) (Fig. 6a). Thirteen analyses from sample XJ-13 (MME within alkali feldspar granite) give similar results and define a weighted-mean $^{206}Pb/^{238}U$ age of 119.6 ± 0.9 Ma (MSWD = 0.52; 2σ) (Fig. 6b). Fifteen concordant analyses from sample XJ-2 (quartz diorite) yield a weighted-mean $^{206}Pb/^{238}U$ age of 110.5 ± 1.0 Ma (MSWD = 0.75; 2σ) (Fig. 6c). Sixteen concordant analyses from sample XJ-5 (quartz diorite) yield a similar weighted-mean $^{206}Pb/^{238}U$ age of 109.3 ± 1.0 Ma (MSWD = 0.54; 2σ) (Fig. 6d). These two ages are identical within analytical error, and can be interpreted as the crystallisation age of the quartz diorites. Twelve analyses from sample XJ-4 (MME within the quartz diorite) are nearly concordant, and yield a weighted-mean $^{206}Pb/^{238}U$ age of 109.5 ± 1.3 Ma (MSWD = 0.33; 2σ) (Fig. 6e). All results from the

MME give ages that overlap with those of their host rocks, indicating that the MME and host rock magmas were coeval.

Twenty analyses from sample BZ-1 (monzogranite) plot as a cluster on the concordia curve, and yield a weighted-mean $^{206}Pb/^{238}U$ age of 109.3 ± 0.9 Ma (MSWD = 0.25; 2σ) (Fig. 6f). Two grains from sample BZ-1 record older $^{206}Pb/^{238}U$ ages of 124 ± 2 and 120 ± 3 Ma, and may be xenocrystic. Six analyses from sample BZ-5 (dolerite) form a near-concordant group with a weighted-mean $^{206}Pb/^{238}U$ age of 110.2 ± 1.5 Ma (MSWD = 0.96; 2σ) (Fig. 6g), which can be interpreted as the crystallisation age of the Beizhang dolerite. Five grains record older $^{206}Pb/^{238}U$ ages of 450 ± 8, 128 ± 6, 120 ± 3, 119 ± 3 and 119 ± 2 Ma, which may represent xenocrysts.

5.1.2. Zircon trace elements and Ti-in-zircon temperatures

The chondrite-normalised REE patterns for all zircons from the Xiaojiang and Beizhang plutons show heavy REE enrichment, positive Ce anomalies (Ce/Ce* = 2.1–1022.3, where $Ce/Ce^* = (La_N \times Pr_N)^{1/2}$ and clear negative Eu anomalies (Eu/Eu* = 0.03–0.80, where $Eu/Eu^* = (Sm_N \times Gd_N)^{1/2}$ (Supplementary Table S2; Fig. 6h), consistent with an igneous origin. However, zircons from different lithologies have highly variable trace element compositions. For example, in the Xiaojiang pluton, the atomic ratio of Zr/Hf in zircon decreases from 82 to 51 (mean = 69) in the quartz diorite, from 75 to 58 (mean = 69) in MMEs within the quartz diorite, from 71 to 43 (mean = 59) in MME within the alkali feldspar granite, and from 78 to 24 (mean = 47)

in the alkali feldspar granite. In the Beizhang pluton, the atomic ratio of Zr/Hf in zircon is 83–60 (mean = 65) and 60–46 (mean = 57) in the dolerite and monzogranite, respectively.

We estimated magmatic temperatures using the Ti-in-zircon thermometer of Ferry and Watson (2007). The TiO_2 activity of crustal rocks is commonly 0.6–0.9, and the SiO_2 activity is typically higher than 0.5 (Ferry and Watson, 2007). Uncertainties associated with the Ti-in-zircon thermometer are >50°C, in which a decrease in the activity of TiO_2, or an increase in the activity of SiO_2, by 0.1, give rise to an increase of ~10°C on the temperature estimates. Considering the absence of rutile and presence of quartz from any of the rocks, activities of TiO_2 and SiO_2 were assumed to be 0.7 and 1, respectively. Calculated Ti-in-zircon temperatures for the alkali feldspar granites and associated MME range from 650°C to 812°C (average = 702°C) and 594°C to 799°C (average = 717°C), respectively (Supplementary Table S2). The monzogranites record similar temperatures (690°C to 736°C; mean = 711°C) as the alkali feldspar granites, and overall are lower than those calculated for the dolerite (658°C to 826°C; mean = 760°C). Nevertheless, the quartz diorites and associated MME show higher Ti-in-zircon temperatures, ranging from 701°C to 909°C (mean = 839°C) and 820°C to 896°C (mean = 861°C), respectively.

5.2. Mineral chemistry

5.2.1. Biotite

Representative electron microprobe analyses of biotites from the Xiaojiang and

Beizhang plutons are listed in Supplementary Table S3. All biotites have low $FeO^T/(FeO^T + MgO)$ values (0.41–0.65) and high MgO contents (11.05–17.06 wt.%). In the Mg–(Al^{VI} + Fe^{3+} + Ti)–(Fe^{2+} + Mn) diagram (Fig. 7a), they are classified as magnesiobiotite. Nevertheless, biotites from the alkali feldspar granite plot close to the boundary between magnesiobiotite and ferrobiotite, whereas those from the quartz diorite plot closer to the phlogopite field. In the Fe^{2+}–Fe^{3+}–Mg diagram (Fig. 7b), most of the samples plot between the nickel–nickel oxide (NNO) and hematite–magnetite (HM) buffers. Samples from all MME and quartz diorites plot above those of the alkali feldspar granite (Fig. 7b), indicating that the MME and quartz diorite formed under more oxidizing conditions.

The concentrations of F and Cl within biotite from the different lithologies show significant compositional variability. Biotites from the alkali feldspar granite and associated MME have distinctly higher F contents (1.06 and 1.90–2.24 wt.%, respectively), whereas biotites from the quartz diorite and associated MME have lower F contents (<0.12 wt.%) and measurable Cl contents (0.26–0.37 wt.%). Concentrations of F and Cl in biotites from the Beizhang pluton are very low. Biotites from the quartz diorite and associated MME have high Ti contents (TiO_2 > 3.69 wt.%), whereas biotites from the alkali feldspar granite and associated MME have lower Ti contents (TiO_2 < 2.80 wt.%), which suggest that biotites from the quartz diorite and associated MME crystallised at higher temperatures than those within the alkali feldspar granite and associated MME.

5.2.2. Feldspar and pyroxene

Representative electron microprobe analyses of feldspars from the Xiaojiang and Beizhang plutons are summarised in Supplementary Table S4 and presented graphically in Fig. 7c. Plagioclase from the alkali feldspar granite and associated MME are albite or oligoclase in composition. However, plagioclase from the quartz diorite and associated MME have relatively high anorthite components and are andesine or bytownite in composition. Plagioclase from the Beizhang pluton is mostly albite, oligoclase or andesine. K-feldspar from the alkali feldspar granite and MME within the Beizhang pluton are mainly orthoclase.

Representative electron microprobe analyses of pyroxenes from the Xiaojiang and Beizhang plutons are summarised in Supplementary Table S5, and presented graphically in Fig. 7d. Pyroxenes from the quartz diorite are diopside, augite or pigeonite, whereas pyroxenes from dolerite are diopside or clinoenstatite. Pyroxenes from MME within the quartz diorite and monzogranite are augite.

5.3. Whole-rock major and trace elements

Representative whole-rock major and trace element analyses from the Xiaojiang and Beizhang plutons are given in Supplementary Tables S6 and S7. Both the alkali feldspar granite and monzogranite have high SiO_2 contents varying from 70.09 to 78.22 wt.% and 69.17 to 73.82 wt.%, respectively. Their corresponding MME have lower SiO_2 contents of 66.16–68.93 wt.% and 56.80 wt.%, respectively. The quartz diorite and associated MME have a relatively low and narrow range of SiO_2 contents

(57.06–60.27 and 56.90–57.92 wt.%, respectively). The dolerite contains the lowest SiO_2 contents (50.34 wt.%). Data for most samples fall into the subalkaline series on a total alkalis vs. silica diagram (Fig. 8a). Notably, all samples from the alkali feldspar granite are ferroan, whereas the other rocks are typically magnesian (Fig. 8b). In the K_2O vs. SiO_2 diagram (Fig. 8c), data for most samples plot within the high-K calc-alkaline series, with the exception of the MME hosted within the alkali feldspar granite, which all belong to the calc-alkaline series. All of the MME have relatively low A/CNK values (<1; Fig. 8d) and are metaluminous. However, the alkali feldspar granite and monzogranite have relatively high and variable A/CNK values of 0.99–1.09 and 0.99–1.11, respectively, and are mostly peraluminous.

All samples from the Xiaojiang and Beizhang plutons have relatively low total REE (ΣREE) concentrations (81.2–234.9 ppm). Chondrite-normalised REE patterns for the alkali feldspar granite and associated MME are marked by significant enrichments in light REE, nearly flat patterns for heavy REE, and variably negative Eu anomalies (δEu = 0.05–0.85 and 0.24–0.92, respectively) (Fig. 9a). In primitive-mantle-normalised multi-element plots (Fig. 9b), the alkali feldspar granite and associated MME show pronounced enrichments in U, Rb, Th, Pb, Zr and Hf, depletions in Ba, Sr, P and Ti, and lack clear negative anomalies in Nb and Ta. In contrast, chondrite-normalised REE patterns for the other rocks exhibit relative enrichment of light REE, and depletion in heavy REE, with high $(La/Yb)_N$ ratios (14.99–21.52), and slightly negative to positive Eu anomalies (δEu = 0.75–1.15) (Fig.

9c). In primitive-mantle-normalised multi-element plots, these rocks show distinct depletions in Nb and Ta, but lack any negative anomalies in Sr, Ba, P, and Ti (Fig. 9d).

5.4. Whole-rock Sr–Nd isotopes

Representative whole-rock Sr–Nd isotopic analyses from the Xiaojiang and Beizhang plutons are given in Table 1 and Fig. 10. Initial $^{87}Sr/^{86}Sr$ ratios (I_{Sr}) and $\varepsilon_{Nd}(t)$ values were calculated based on the measured zircon U–Pb ages. All rocks from the Xiaojiang and Beizhang pluton have uniform I_{Sr} values (0.7078 to 0.7084) and $\varepsilon_{Nd}(t)$ values (–5.75 to –4.50). On a plot of $\varepsilon_{Nd}(t)$ vs. age (Fig. 10a), all samples lie above the evolutionary trend defined by the Proterozoic crustal basement rocks from the South China Block. The samples also have comparatively young two-stage Nd model ages (T_{DM2} = 1.29–1.37 Ga).

5.5. Zircon Hf isotopes

In situ zircon Hf isotopic compositions from the Xiaojiang and Beizhang plutons are listed in Supplementary Table S8 and illustrated in Fig. 10b. For the calculation of $\varepsilon_{Hf}(t)$ and T_{DM2} values, *in situ* zircon U–Pb ages were used. Zircons from the alkali feldspar granite and quartz diorite have similar Hf isotopic compositions with $\varepsilon_{Hf}(t)$ values ranging from –7.5 to –2.5 and –8.1 to –2.7, respectively. Their corresponding enclaves have similar but relatively homogeneous zircon Hf isotopic compositions, with $\varepsilon_{Hf}(t)$ values of –5.2 to –2.1 and –6.2 to –4.5, respectively (Fig. 10b). Excluding those zircons within the monzogranite with unusually low $\varepsilon_{Hf}(t)$ values (–13.1), the monzogranite and dolerite have similar Hf isotopic signatures, with $\varepsilon_{Hf}(t)$ values of –

5.8 to –3.3 and –5.3 to –2.4, respectively. Overall, most zircons from the Xiaojiang and Beizhang plutons plot above the Hf isotope evolutionary array defined by crustal basement rocks from the Cathaysia Block in a $\varepsilon_{Hf}(t)$ vs. age diagram (Fig. 10b). Moreover, with the exception of one zircon (BZ-1-05) that shows a much older two-stage Hf model age (T_{DM2} (Hf) = 1.96 Ga), most zircons from the Xiaojiang and Beizhang plutons have younger T_{DM2} (Hf) ages of 1.28–1.67 Ga.

6. Discussion

6.1. Petrogenesis of the ferroan and magnesian granitoids

6.1.1. Petrogenetic classification of the magnesian and ferroan granitoids

The magnesian granitoids (quartz diorite and monzogranite) from the Xiaojiang and Beizhang plutons contain hornblende but no typical alkaline mafic minerals (e.g., arfvedsonite, riebeckite, and aegirine–augite) or peraluminous minerals (e.g., cordierite, andalusite, and garnet). The magnesian granitoids have relatively low SiO_2 contents (<74 wt.%), high K_2O contents (Fig. 8c), and are metaluminous, mostly with A/CNK ratios of 0.80 to 1.0 (A/CNK = 1.11 for sample BZ-6). The FeO_T/MgO ratios (1.90–3.66) of these rocks are much lower than in typical A-type granites (ca. 13.4; Whalen et al., 1987). The geochemical characteristics detailed above suggest that the magnesian granitoids are high-K calc-alkaline I-type granitoids.

In contrast, the ferroan granites (Xiaojiang alkali feldspar granites) have evolved SiO_2 contents (up to 78.22 wt.%) and high differentiation index (D.I.) values (93.3–97.1). They consist of quartz, K-feldspar, plagioclase and minor biotite but lack

hornblende, and are close to haplogranitic compositions. Their weakly peraluminous (A/CNK = 0.99–1.09) characteristics are distinct from those of strongly peraluminous S-type granites (A/CNK > 1.1). The P_2O_5 abundances in the ferroan granites decrease with increasing SiO_2 and are <0.01 wt.% at SiO_2 = 76.47–77.23 wt.%, analogous to typical I-type granites. The alkali feldspar granites are low in Al_2O_3, MgO or CaO and high in K_2O, similar to A-type granites (Huang et al., 2011). However, they have variable Zr + Nb + Ce + Y contents (150.0–418.4 ppm), and low Ga/Al * 10000 (<2.6) and FeO_T/MgO ratios (5.86–12.73), which differ from typical A-type granites (Whalen et al., 1987). Therefore, both the magnesian and ferroan granites from the Xiaojiang and Beizhang plutons are classified as I-type granites.

6.1.2. Potential magma sources for the magnesian and ferroan granitoids

The negative zircon $\varepsilon_{Hf}(t)$ values (–13.1 to –2.5) combined with the evolved whole-rock Sr–Nd isotopic compositions (I_{Sr} = 0.7078–0.7080; $\varepsilon_{Nd}(t)$ = –5.75 to –4.99) of the Xiaojiang and Beizhang granitoids indicate reworking of an older crustal component. Because almost all zircons from these granitoids give Palaeo- to Mesoproterozoic crustal model ages (1.65 to 1.31 Ga, excluding one with an age of 1.96 Ga), we speculate that the magmatic sources may have predominantly comprised Mesoproterozoic or Palaeoproterozoic rocks. The existence of zircon with unusually low $\varepsilon_{Hf}(t)$ values (–13.1) within the monzogranite may support the involvement of Palaeoproterozoic materials. However, the majority of the Nd and Hf model ages from those granitoids are much younger than those of the basement rocks (Fig. 10b)

(>1.85 Ga; Xu et al., 2007). Meanwhile, existing zircon data (including U–Pb dating and Lu–Hf isotopic analyses) from Neoproterozoic sediments in the region revealed five main episodes of juvenile crust generation at 3.6, 2.8, 2.6–2.4, 1.85 and 0.8–0.7 Ga (Yu et al., 2010). Thus, most zircon Hf model ages from the Xiaojiang and Beizhang granitoids do not correspond with any previously reported episodes of crust generation. Consequently, the Hf model ages are unlikely to be geologically meaningful, but rather reflect mixing between magmas derived from a juvenile source (i.e., the mantle or Neoproterozoic crust), and magmas largely derived by remelting of Palaeoproterozoic materials (Paleoproterozoic basement rocks/recycled Paleoproterozoic materials).

Patiño Douce (1999) showed that the relative behaviour of alumina and mafic components differs notably amongst experimentally produced partial melts of metagreywackes, metapelites and amphibolites. Melts of mica-rich sources have a relatively restricted range of $Al_2O_3 + FeO + MgO + TiO_2$ contents, but a wide range of $Al_2O_3/(FeO + MgO + TiO_2)$ ratios. The opposite is true for partial melts of amphibolite (Fig. 11a). According to Fig. 11a, the source rocks of the alkali feldspar granites were most likely metamorphosed pelites with a minor greywacke component, whereas the monzogranites were generated mainly by partial melting of metamorphosed greywackes. On the molar K_2O/Na_2O vs. molar $CaO/(MgO + FeO_T)$ diagram (Fig. 11b), the alkali feldspar granites plot in the fields of metapelites, metagreywackes and metaandesites, and most monzogranites plot in the fields of

metaandesites. Therefore, both granites require quartzofeldspathic crust as their source rocks. The variable Th/Nb and Th/Yb ratios for the alkali feldspar granites and monzogranites support some involvement of metasedimentary source rocks in their genesis (Ribeiro et al., 2013) (Fig. 11c–d). The alkali feldspar granites and monzogranites exhibit weakly peraluminous characteristics that can also be ascribed to the input of metasedimentary material during their formation Nevertheless, the quartz diorites have low $Al_2O_3/(FeO + MgO + TiO_2)$ and molar K_2O/Na_2O ratios, and high $Al_2O_3 + FeO + MgO + TiO_2$ values, consistent with basaltic source rocks (Fig. 11a–b).

6.2. Mantle contributions and the role of magma mixing

6.2.1. Petrogenesis of the Beizhang mafic dyke

The Beizhang dolerite dyke (sample BZ-5) is characterised by low SiO_2 (50.34 wt.%), and high MgO (6.46 wt.%), Mg# (60) and compatible element contents (e.g., Cr = 206 ppm and Ni = 113 ppm), suggesting that it was derived from a mantle source. The Ba (1010 ppm) and Sr (912 ppm) concentrations in the dolerite are much higher than those of average continental crust (Ba = 390 ppm; Sr = 325 ppm) (Rudnick and Fountain, 1995), suggesting these trace elements were not affected by significant crustal contamination. The low La/Yb ratio (0.14) for the dolerite sample support only a limited degree of crustal contamination. The dolerite has high I_{Sr} and low $\varepsilon_{Nd}(t)$ values (0.707901 and –4.50, respectively). Such signatures, in conjunction with the other chemical characteristics (e.g., high K_2O contents and significant large-ion

lithophile element (LILE) and light REE enrichment; Fig. 9c–d), require a contribution from an enriched mantle source. Consequently, marked depletions in Nb and Ta in the primitive-mantle-normalised multi-element diagram indicate that the magma was derived from a source with elevated LILE and light REE, consistent with a contribution from slab-derived hydrous fluids or melts.

With respect to slab-derived components, trace element ratios play a crucial role in discriminating between aqueous fluids and silicate melts [i.e., using ratios of fluid or melt mobile element (Rb, Ba, Cs, La and Th) over fluid immobile element (Ta, Nb, Sm and Yb); Pearce et al., 2005]. Amongst these elements, La and Th are only mobile within melts of sediment, whereas Rb, Ba and Cs are mobilised in both aqueous fluids and deeper melts of sediment (Ribeiro et al., 2013). As a consequence, the composition of any subduction component can be tracked using Ba/Nb and Ba/Yb ratios, and the shallower aqueous fluids can be tracked by Rb/Th, Ba/Th and Cs/Th ratios (Pearce et al., 2005; Ribeiro et al., 2013).

In this study, the data suggest a significant role for slab-derived hydrous fluids, but only negligible involvement of sediments in the mantle source region, as evidenced by high Ba/Th and Sr/Nd ratios and low Th/Nb and Th/Yb ratios in the Beizhang mafic dyke (Fig. 11c–d). The relative depletion in Y and heavy REE reflects either derivation of the metasomatic agent from a garnet-rich source or fractionation of garnet during partial melting of the mantle. Previous studies have shown that partial melting in the garnet stability field will produce melts with high Dy/Yb ratios

(>2.5), whereas melting in the spinel stability field will generate melts with low Dy/Yb ratios (<1.5) (Jiang et al., 2009). The dolerite has a Dy/Yb ratio of 2.2, implying that partial melting may have taken place within the spinel–garnet transition zone (at a depth of 75–85 km) (Jiang et al., 2009) or that the dolerite reflects mixing between melts derived from different depths (Liu et al., 2014).

6.2.2. Petrogenesis of the MME

Several interpretations have been proposed for the petrogenesis of MME, including: (1) refractory metamorphic rocks, recrystallised fragments or melt residues from the granite source (Chappell et al., 1987); (2) wall-rock xenoliths (Maas et al., 1997); (3) cognate fragments of early formed crystals or cumulate minerals from the host magma (Donaire et al., 2005); (4) globules of a more mafic magma that was injected into, and mingled and/or mixing with, the host granitic magma (Griffin et al., 2002; Liu et al., 2013).

All the Xiaojiang and Beizhang MME have relatively high Na_2O contents (4.07–6.24 wt.%), are metaluminous (A/CNK = 0.82–0.98), and lack typical peraluminous minerals (e.g., garnet, andalusite or cordierite) or inherited zircon, which contradict the restite model (Chappell et al., 1987). The identical zircon U–Pb ages recorded by the MME and their host granitoids argue against both a restite and xenolith origin for the MME, suggesting they have either a hybrid or cognate origin. However, all MME are much smaller than their host granitoids in mineral grains and no cumulate textures have been recognised, precluding a cognate origin. In addition, the similarity in the

ΣREE concentrations and the sub-parallel REE patterns for the MME and host granitoids conflict with an cognate model.

Consequently, we propose that the MME from the Xiaojiang and Beizhang plutons represent globules of a more mafic magma that mingled and mixing with the host granitic magma. Several lines of evidence support this hypothesis: (1) petrological observations (e.g., most MME show rounded to elongated shapes and fine-grained textures with lobate margins; back-veining and feldspar xenocrysts occur within some MME; Fig. 3b–e); (2) microstructural observations demonstrate that acicular apatite and disequilibrium textures (e.g., plagioclase grains with oscillatory zoning that are partially resorbed) are widely developed within the MME (Fig. 4d–g), indicating changes in the chemical and/or thermal conditions due to magma mixing; (3) differences in geochemistry between the alkali feldspar granites and MME, indicating that the MME are likely to be exotic (i.e., the alkali feldspar granites are ferroan high-K calc-alkaline rocks, whereas the associated MME are magnesian calc-alkaline rocks); (4) differences in the inferred source rocks for the MME and their host granites (e.g., the MME samples are classified as amphibolite-derived melts, unlike the alkali feldspar granites and monzogranites; Fig. 11a–b); (5) the composition of the coeval Beizhang dolerite dyke (ca. 110 Ma) indicates the involvement of mantle-derived magmas in the formation of the quartz diorite and monzogranite; (6) all MME have higher Mg# values than those rocks entirely derived from partial melting of crustal materials (Fig. 11e; Jiang et al., 2013 and references

therein), requiring input of mantle-derived components; and (7) the wide range in zircon Hf isotopic compositions in the MME and their host rocks preclude a simple cogenetic evolution via closed-system fractionation (Yang et al., 2007). Thus, the MME from the Xiaojiang and Beizhang plutons probably represent derivatives of mantle-derived mafic magmas that intruded partially crystallised, crustally derived silicic magmas.

6.2.3. Two episodes of mafic magmatism

As discussed above, two major episodes of mafic magmatism were involved in the genesis of the granitoids based on their magmatic ages—Stage 1 (the ca. 120 Ma MME within the alkali feldspar granites) and Stage 2 (the ca. 110 Ma mafic dykes and MME within the quartz diorites and monzogranites). The subcontinental lithospheric mantle (SCLM) of south China has been suggested to have an EM-II type isotopic signature (He et al., 2010). However, all zircons from the Stage 1 and 2 MME and mafic dykes have much higher $\varepsilon_{Hf}(t)$ values (–5.2 to –2.1, –6.2 to –4.5 and –5.3 to –2.4, respectively) than enriched mantle (average = –10.3; He et al., 2010), providing evidence for the participation of depleted mantle in the petrogenesis of the two generations of mafic magmas.

The Stage 1 MME have relatively high initial $^{87}Sr/^{86}Sr$ ratios (0.708354) and low $\varepsilon_{Nd}(t)$ values (–4.88), low La/Nb ratios (1.1–1.3), and depletions in Sr, Ba, P and Ti, but no obvious depletions in Nb and Ta (Fig. 9). Minor assimilation of slab-derived fluids or sediments is suggested by the low Th/Yb, Th/Nb, Ba/Th and Sr/Nd ratios of

Stage 1 MME (Fig. 11c–d). Overall, these geochemical features are very similar to 160–110 Ma basaltic rocks from the interior regions of the SCB, which are thought to have formed by mixing of melts from the SCLM and asthenospheric mantle (Meng et al., 2012).

However, the higher heavy REE contents for Stage 1 MME compared with contemporaneous basaltic rocks requires explanation. Notably, rocks from the alkali feldspar granite and its enclaves have F-rich compositions, as revealed by the widespread occurrence of F-bearing biotite. Two main models have been advanced, suggesting that such F either has a primary magmatic origin (Dostal and Chatterjee, 1995) or was the result of secondary metasomatism (Nurmi and Haapala, 1986). Considering the sharp intrusive contacts between the alkali feldspar granites and host country rocks, as well as the lack of evidence for any metasomatic effects in the rocks, we favour a magmatic origin for the F. The halogens (F or Cl) remain dissolved within the magma, lowering the crystallisation temperature, which cause REEs and high-field-strength elements (HFSE) to form complexes and behave as incompatible elements (Moghazi et al., 2011). Such behaviour can explain the high and variable contents of REE and HFSE in the alkali feldspar granites and their MME.

The Stage 2 MME and mafic dykes are characterised by distinct negative Nb and Ta anomalies, relatively high La/Nb ratios (3.0–4.3), and similar initial $^{87}Sr/^{86}Sr$ ratios (0.707901 to 0.707907) and $\varepsilon_{Nd}(t)$ values (–4.50), which together define a strong arc signature. Moreover, the Stage 2 MME and mafic dyke samples do not show a

negative correlation between $\varepsilon_{Nd}(t)$ and La/Nb. This argues against crustal contamination, and requires a component with relatively high $\varepsilon_{Nd}(t)$ values and La/Nb ratios in the formation of these magmas. Taken together, these characteristics are similar to 110–77 Ma Cretaceous basaltic rocks in the coastal region of the Cathaysia Block (Fig. 11f), reflecting a contribution from a subduction-related component (Meng et al., 2012). The subduction-related component may be melts derived either from newly formed SCLM that was formerly metasomatised by slab-derived melts/fluid, or components produced during slab subduction. Significant addition of slab-derived fluids with a minor contribution from sediments is inferred for the source of Stage 2 MME and mafic dykes based on their variable Ba/Th and Sr/Nd ratios and mainly constant Th/Yb and Th/Nb ratios (Fig. 11c–d). Considering that SCLM components were involved in both episodes of mafic magmatism in the region, we suggest that the fluids were derived directly from the downgoing slab at 120–110 Ma.

In summary, we suggest that the source for Stage 1 MME magmas was mainly the SCLM with some contribution from asthenospheric mantle (Fig. 11f), whereas the Stage 2 (110 Ma MME and mafic dykes) mafic magmas were derived from mixing of SCLM- and asthenosphere-derived melts that were simultaneously metasomatised by slab-induced fluids.

6.3. The causes of iron enrichment or depletion in the granitoids

Both ferroan (alkali feldspar granite) and magnesian (monzogranite) granitoids require quartzofeldspathic crust as their main source rocks. However, the causes of

iron enrichment or depletion in these granitoids is unclear. The oxidation state of the magmas is a likely factor in controlling iron enrichment in the ferroan granitoids relative to their magnesian counterparts (Dall'Agnol et al., 2017; Zhu et al., 2016).

The Ce^{4+}/Ce^{3+} ratio as measured in zircon is considered to be a measure of the oxidation state of magmas (Ballard et al., 2002; Liang et al., 2006), but is temperature dependent, for which lower magmatic temperatures lead to higher Ce^{4+}/Ce^{3+} ratios (Liang et al., 2006). Considering the distinctly different magmatic temperatures inferred for the ferroan and magnesian granitoids, we used the new calibration method of Smythe and Brenan (2016) to estimate oxygen fugacities ($\log fO_2$) based on zircon, which depends on the temperature, $Ce^{3}+/Ce^{4+}$ ratio of the melt and water content. In this method, the $Ce^{3}+/Ce^{4+}$ ratios of the melts were calculated using a lattice strain model based on both the whole-rock and zircon trace element compositions (Ballard et al., 2002). The temperature of the melt was obtained using the Ti-in-zircon thermometer.

As discussed previously, the Cretaceous igneous rocks exposed along the coastal area are generally accepted to be related to subduction of the paleo-Pacific plate (Zhou et al., 2006). Considering that the water contents of arc magmas are 2–6 wt.% (mean = 4 wt.%) (Plank et al., 2013), a H_2O concentration of 4 wt.% was assumed. In the Xiaojiang pluton, the oxygen fugacities ($\log fO_2$) estimated for the alkali feldspar granite and associated MME are FMQ –1.8 to +1.9 and FMQ –1.7 to +3.1, respectively. These are lower than those calculated for the quartz diorite (FMQ –0.6 to

+2.1) and MME within the quartz diorite (FMQ –0.4 to +1.1). In the Beizhang pluton, the calculated oxygen fugacities (logfO_2) for the monzogranite and dolerite are FMQ +0.5 to +1.7 (with the exception of one zircon with logfO_2 = FMQ –1.6) and FMQ –0.6 to +1.2, respectively. The analytical errors, including those associated with the whole-rock major and trace element analyses, and the zircon trace element analyses, equate to an uncertainty of logfO_2 = 1.2 on average.

The estimated oxygen fugacity for the ferroan alkali feldspar granites and associated MME shows significant variations (Fig. 12a), which may imply conditions of crystallisation changed as a result of magma mixing and mingling. Some zircon grains from the ferroan granitoids record significantly more reducing conditions (down to FMQ –1.8). In contrast, the magnesian granitoids (quartz diorite and monzogranite) crystallised under more oxidizing conditions, estimated respectively at FMQ –0.6 to +2.1 and FMQ +0.5 to +1.7 (Fig. 12a; Supplementary Table S2).

Smythe and Brenan (2016) have proposed that estimates of logfO_2 are sensitive to changes in H_2O content, and that if a completely anhydrous composition is assumed, the resulting fO_2 would be 2.5 to 3 log units lower than for the same melt with ~5 wt.% H_2O. As detailed earlier, significant slab-derived fluids were involved in the formation of the magnesian granitoids and associated MME, whereas negligible or only minor fluid additions were involved in formation of the alkali feldspar granites and associated MME. Therefore, assuming an identical H_2O content of 4 wt.% for all magmas would be inappropriate. The water contents in the magmas of

magnesian granitoids is likely to be higher than 4 wt.% based on the observation that amphibole is commonly the main mafic mineral in such rocks (Dall'Agnol et al., 2017). The presence of plagioclase with relatively high An numbers within the magnesian granitoid and associated MME is also typical of parental magmas with high water contents (Fig. 7c) (Waters and Lange, 2015).

In contrast, the water contents of the ferroan granitoids are likely to have been less than 4 wt.% based on the absence of amphibole and scarcity of euhedral biotite. The ferroan granitoids show significant depletion in Sr and Eu, perhaps caused by the high melting point of plagioclase under dry conditions (Zhu et al., 2016). Based on the above considerations, we assume H_2O contents of 2 wt.% for the ferroan granitoids and associated MME, and 6 wt.% for the magnesian granitoids, and their associated MME and the mafic dykes. Using these H_2O contents, we estimate the possible range of fO_2 for the ferroan granitoid and associated MME to lie between FMQ –2.7 to +1.0 and FMQ –2.6 to +2.2, respectively (Fig. 12b). The range in fO_2 calculated for the magnesian granitoid, and associated MME and mafic dyke is more oxidizing (FMQ +0.2 to +3.0; except for an FMQ of –0.8 for one zircon within the monzogranite; Fig. 12b). Notably, some zircon grains within the MME record more oxidizing conditions (up to FMQ +2.2) than those within the host alkali feldspar granites, implying that the high oxygen fugacities were inherited from the more hydrous mantle-derived mafic magmas.

Given that V is more incompatible in ferromagnesian minerals under high

oxygen fugacities, the concentration of V relative to other transition metals can be used as a qualitative estimate of fO_2 (Zhu et al., 2016 and references therein). The much lower V/Sc ratios recorded by the alkali feldspar granites (0.38−3.17) and associated MME (2.41−2.44) relative to the magnesian granitoids (3.83−10.00) indicate more reduced conditions in the former. Moreover, the calculated zircon oxygen fugacities are consistent with those deduced based on the content of biotite (Fig. 7b).

High oxygen fugacities can promote the formation of magnetite and consequently inhibit enrichment of the melt in iron, whereas low oxygen fugacity may result in the formation of fayalite and high-Fe residual melts (Zhu et al., 2016). However, Chiaradia (2015) showed that crustal thickness exerts a first order control on the Sr/Y variability of arc magmas, and that the development of both calc-alkaline and high Sr/Y signatures are primarily the result of intracrustal processes (e.g., the early fractionation of magnetite and amphibole and suppression of plagioclase fractionation at high pressure). The Gd/Yb ratio may be also used as an index of the pressure of melting—a high Gd/Yb ratio reflects the presence of garnet at high crustal pressures. For pressure-moderated iron depletion in arc magmas, oxygen fugacity should be above FMQ to stabilise magnetite (Behrens and Gaillard, 2006). For the Xiaojiang and Beizhang granitoids, the control of oxygen fugacity on iron enrichment in the alkali feldspar granites is suggested by oxygen fugacities (down to FMQ –2.7) and V/Sc ratios that are lower than those recorded in the magnesian granitoids (above

or equal to the FMQ buffer). The fact that the ferroan granitoids also have much lower Gd/Yb (0.50–2.63) and Sr/Y (0.1–2.9, with one highly elevated value of 30.7 in sample XJ-1) ratios than the magnesian granitoids (Gd/Yb = 1.44–3.28; Sr/Y = 26.2–53.6), implies that fractionation/melting pressures can also have played an important role. Therefore, the iron enrichment/depletion in the Xiaojiang and Beizhang granitoids was mainly controlled by two factors, which were oxygen fugacity and pressure.

6.4. Implications for the geodynamics of paleo-Pacific plate subduction

The ferroan granitoids (i.e., the ca. 120 Ma alkali feldspar granites) have low Gd/Yb (0.50–2.63) and Sr/Y (0.1–30.7) ratios and low crystallisation temperatures. Their inferred lower pressures of melting together with the requirement for a quartzofeldspathic crustal source imply that the ferroan granitoids were generated by partial melting of rocks in the middle to upper continental crust. In contrast, the magnesian granitoids (i.e., the ca. 110 Ma quartz diorites) have higher Gd/Yb (2.75–3.28) and Sr/Y (50.0–53.6) ratios and record higher temperatures. As they are inferred to have had metabasaltic source rocks, they were probably derived from the lower crust. Other magnesian granitoids (i.e., the ca. 110 Ma monzogranites,) have intermediate Gd/Yb (1.44–2.54) and Sr/Y (26.2–45.1) ratios and record intermediate temperatures (Fig. 12), and may have been generated by partial melting of quartzofeldspathic crust at deeper levels than those inferred for generation of the alkali feldspar granites.

The older ferroan granitoids (ca. 120 Ma) record lower melting temperatures, pressures, water contents and oxygen fugacities than the ca. 110 Ma magnesian granitoids, reflecting a change in tectonic regime. In this study, similar source rocks for the alkali feldspar granites and monzogranites suggest that the strong variations in oxygen fugacity were mainly controlled by mixing of external materials with variable water contents. The Xiaojiang and Beizhang granitoids show variable and positively related oxygen fugacities and water contents, consistent with the typical products of a subduction zone, where H_2O-rich and oxidizing conditions result from the effects of the subducting slab.

The ferroan granitoids (120 Ma) in the Xiaojiang area record low melting pressures and are interpreted to have formed in an extensional tectonic setting, similar to other ferroan granitoids worldwide. The ferroan granitoids also exhibit geochemical signatures similar to the contemporaneous 125 Ma Baijuhuajian A-type granite located in the neighbouring interior region. These features include high $FeO_T/(FeO_T + MgO)$ and K_2O/Na_2O ratios, enrichment in Th, Rb, Pb and U, depletion in Sr, Ba, P and Ti, and an absence of clear Nb and Ta anomalies (Wong et al., 2009). The Baijuhuajian granite has high zircon $\varepsilon_{Hf}(t)$ values (–0.5 to +4.2) and is considered to have been originally derived from the asthenospheric mantle that then underwent extensive crystal fractionation along with limited contamination with crustal components (Wong et al., 2009). Ferroan granitoids in this study have lower $\varepsilon_{Hf}(t)$ values (–7.5 to –2.5), and were derived from mixing between quartzofeldspathic,

crustally derived melts with subordinate mantle-derived basaltic magmas. Along with many other A-type granites (e.g., the 136–124 Ma Suzhou, Fuling, Tongshan, Damaoshan, Lingshan and Mikengshan intrusions) (Jiang et al., 2015; 2011; Qiu et al., 2006; Wong et al., 2009; Zhou et al., 2013), those studied here provide evidence for extension in the interior–coastal regions of southeastern China at 136–120 Ma (Li et al., 2014a).

Igneous rocks related to extension at 101–83 Ma are widespread in the coastal areas of southeastern China, including A-type granites, mafic dykes and bimodal volcanic rock associations (Li et al., 2014b; Zhao et al., 2016). These indicate migration of the regional extension from inland areas towards the coast after 101 Ma. However, controversy remains concerning the tectonic setting of the interior–coastal regions during the period 120–101 Ma. For example, Wong et al. (2009) suggested there was continued local extension from 125 to 100 Ma due to slab rollback and/or break-off of the subducting paleo-Pacific plate. Based on the study of several Cretaceous syenitic and gabbroic rocks, He and Xu (2012) proposed that there was a transition from compression to extension at ca. 110 Ma, corresponding to a transition from subduction advance to subduction retreat (rollback). Actually, the upper and lower volcanic series in Fujian and Zhejiang provinces record a period of tectonic transition at ca. 110 Ma (He and Xu, 2012 and references therein). Major drawbacks to the above two models are incompatibilities in the confirmed geological facts (extension during 136–120 Ma and changed tectonic regime during 120–101 Ma).

Wang et al. (2011) showed that 180–125 Ma igneous rocks in the SCB become gradually younger towards the northeast. Recently, a trend of younging towards the northeast has been recognised in the 145–127 Ma lower volcanic series (Liu et al., 2016b), implying an increase in the dip of the subducting slab from southwest to northeast. Therefore, the Pacific Plate could have been moving towards the southwest at 145–127 Ma. It is worth noting that the entire upper volcanic series in southeastern China was produced at 110–88 Ma and is mainly distributed in the coastal area (Liu et al., 2016b). Moreover, the abundance of 101–83 Ma extension-related rocks imply a peak in regional lithospheric extension during the Late Cretaceous in response to rollback of the paleo-Pacific plate (Zhao et al., 2016). Thus, the direction of motion of the paleo-Pacific plate at 110–88 Ma would have been towards the northwest, as suggested by most previous studies (He and Xu, 2012; Jiang et al., 2015; Li et al., 2014a, b; Liu et al., 2016b). In summary, the direction of motion of the subducting paleo-Pacific plate may have changed during the period 127 to 110 Ma. Based on the tracks of ocean island volcanic chains, Sun et al. (2007) have proposed that the change in the direction of motion of the paleo-Pacific plate occurred at ca. 125–122 Ma.

A compilation of our new data and previously published geochemical data from Cretaceous igneous rocks considered to include mantle components in their origin (Charoy and Raimbault, 1994; Griffin et al., 2002; He and Xu, 2012; Jiang et al., 2011; Li et al., 2012, 2016; Liu et al., 2013, 2014a, 2016a; Qi et al., 2016; Qiu et al., 2006,

2012; Wong et al., 2009; Zhou et al., 2013), excluding those derived mainly from crustal rocks, demonstrates that the 132–119 Ma igneous rocks in southeastern China record minimal addition of slab-derived components in their magma sources (Fig. 13a–b). This finding agrees with a change in the direction of motion of the subducting paleo-Pacific plate during this period. In contrast, the asymmetric paleo-Pacific slab rollback model proposed by Liu et al. (2016b) for the period 150–120 Ma cannot explain the minimal addition of slab-derived components in the formation of most 132–119 Ma igneous rocks in southeastern China. The Mikengshan granite exhibits much lower Ba/Nb and La/Nb ratios than the contemporary Caiyuan syenite, which is also in accordance with southwest-directed subduction of the paleo-Pacific plate at 136 Ma. The involvement of voluminous slab-derived components in the manle source rocks of the 118 Ma Huangtuling syenite, 110 Ma Xiaojiang–Beizhang magnesian granitoids, 109–95 Ma monzonites (Kanggu, Huangtanyang, Matou, Dalai and Jintonghu) (Fig. 13) and 110–100 Ma basaltic rocks (Fig. 11f) can be explained by rapid high-angle rollback of the subducting paleo-Pacific plate after 119 Ma. Consequently, the major changes in Ba/Nb and La/Nb values after 136 Ma suggest that onset of the change in direction of the paleo-Pacific plate could have been later than 136 Ma, and most likely occurred at ca. 125 Ma (Sun et al., 2007).

Taking all of these considerations into account, the distribution of the Cretaceous igneous rocks can be attributed to a change in the direction of motion of the paleo-Pacific plate. The inferred minimal contribution of slab-derived components at

132–119 Ma was probably caused by the transition of the direction of subduction from the southwest to northwest at ca. 125–122 Ma (Sun et al., 2007; Wang et al., 2011), which is a conclusion supported by this study. The 132–119 Ma igneous rocks that occur in the interior coastal regions (including the Xiaojiang ferroan granitoids and associated MME) were formed in this tectonic regime under relatively H_2O-poor and low oxygen fugacity conditions. During rollback of the subducted slab after 118 Ma, dehydration or partial melting of the downgoing oceanic crust produced voluminous H_2O-rich fluids that promoted melting of upwelling asthenospheric mantle and the subsequent production of underplated basalts. The 118–95 Ma igneous rocks in the coastal area (including the Huangtuling syenite, Xiaojiang–Beizhang magnesian granitoids, Kanggu, Huangtanyang, Matou, Dalai and Jintonghu monzonites, and some basaltic rocks) were formed during this period under conditions characterised by distinctly higher water contents and oxygen fugacities.

7. Conclusions

The results of zircon U–Pb dating imply that ferroan and magnesian granitoids from the Xiaojiang–Beizhang area were emplaced during the Cretaceous at ca. 120 and 110 Ma, respectively. The MME and mafic dykes are coeval with their host granitoids. The granitoids were produced by partial melting of crustal rocks and mixed and mingled with mantle-derived magmas. The MME probably represent derivatives of mantle-derived magmas that intruded the crustally derived granitic magmas. Two episodes of mafic magmas were involved in granitoid genesis. The

mafic sources for Stage 1 (the 120 Ma MME) were mainly the SCLM with some involvement from the asthenospheric mantle; the parental magmas for Stage 2 (the 110 Ma MME and mafic dykes) were mafic melts derived from both the SCLM and asthenosphere that were simultaneously metasomatised by slab-derived fluids. Iron enrichment or depletion in the Xiaojiang and Beizhang granitoids was mainly controlled by two factors: oxygen fugacity and pressure.

The older ferroan granitoids record lower melting temperatures, pressures, water contents and oxygen fugacities than the younger magnesian granitoids, reflecting a change in the tectonic regime in which they formed. Our new data, combined with previously published data from Cretaceous igneous rocks in southeastern China, reveal major geochemical changes at 136 and 118 Ma, respectively. The 132–119 Ma igneous rocks in southeastern China record minimal addition of slab-derived components to their magmatic sources, and provide strong evidence that the direction of motion of the paleo-Pacific plate changed from southwest to northwest at ca. 125–122 Ma.

Acknowledgements

We thank Editor Prof. Nelson Eby, Dr. Kong-Yang Zhu and an anonymous reviewer for their thoughtful comments and constructive suggestions which greatly improved the manuscript. We also thank Dr. Zhi-Hui Dai, Dr. Jian-Xin Zhao, Dr. Yue-Xing Feng and Mr. Xiang Li for their help with the analyses and technical assistance. This study was financially supported by the National Key R&D Program

of China (2016YFC0600405), the National Natural Science Foundation of China (Grant No. 41602060, 41702048), and Chinese Academy of Sciences (CAS) "Light of West China" program.

Supplementary Table S1. Zircon LA-ICP-MS U–Pb dating results of the Xiaojiang and Beizhang plutons

Supplementary Table S2. Trace elements (ppm) in zircon from the Xiaojiang and Beizhang plutons acquired by LA-ICP-MS

Supplementary Table S3. Representative microprobe analyses of biotites from the Xiaojiang and Beizhang plutons

Supplementary Table S4. Representative microprobe analyses of feldspars from the Xiaojiang and Beizhang plutons

Supplementary Table S5. Representative electron-microprobe analyses of pyroxenes from the Xiaojiang and Beizhang plutons

Supplementary Table S6. Major element contents (wt.%) of representative samples from the Xiaojiang and Beizhang plutons

Supplementary Table S7. Trace and rare earth element (ppm) analyses of representative samples from the Xiaojiang and Beizhang plutons

Supplementary Table S8. Zircon in-situ Hf isotopic compositions from the Xiaojiang and Beizhang plutons

The following are the supplementary data related to this article.

Supplementary material 1

References

Altherr, R., Siebel, W., 2002. I-type plutonism in a continental back-arc setting: Miocene granitoids and monzonites from the central Aegean Sea, Greece. Contributions to Mineralogy and Petrology 143(4), 397–415.

Ballard, J.R., Palin, M.J., Campbell, I.H., 2002. Relative oxidation states of magmas inferred from Ce(IV)/Ce(III) in zircon: application to porphyry copper deposits of northern Chile. Contributions to Mineralogy and Petrology 144(3), 347–364.

Behrens, H., Gaillard, F., 2006. Geochemical aspects of melts: Volatiles and redox behavior. Element 2(5), 275–280.

Bouvier, A., Vervoort, J.D., Patchett, P.J., 2008. The Lu–Hf and Sm–Nd isotopic composition of CHUR: Constraints from unequilibrated chondrites and implications for the bulk composition of terrestrial planets. Earth and Planetary Science Letters 273(1–2), 48–57.

Boynton, W.V., 1984. Geochemistry of the rare earth elements: meteorite studies. In: Henderson, P. (Ed.), Rare Earth Elements Geochemistry, Elsevier, Amsterdam.

Chappell, B.W., White, A.J.R., 1974. Two contrasting granite types. Pacific Geology 8, 173–174.

Chappell, B.W., White, A.J.R., Wyborn, D., 1987. The Importance of Residual Source Material (Restite) in Granite Petrogenesis. Journal of Petrology 28(6), 1111–1138.

Charoy, B., Raimbault, L., 1994. Zr-Rich, Th-Rich, and Ree-Rich Biotite Differentiates in the a-Type Granite Pluton of Suzhou (Eastern China) - the Key Role of Fluorine. Journal of Petrology 35(4), 919–962.

Chen, C.H., Lee, C.Y., Shinjo, R., 2008. Was there Jurassic paleo-Pacific subduction in South China?: Constraints from 40Ar/39Ar dating, elemental and Sr–Nd–Pb isotopic geochemistry of the Mesozoic basalts. Lithos 106(1–2), 83–92.

Chiaradia, M., 2015. Crustal thickness control on Sr/Y signatures of recent arc magmas: an Earth scale perspective. Scientific Reports 5, 8115.

Dall'Agnol, R. et al., 2017. Mineralogy, geochemistry, and petrology of Neoarchean ferroan to magnesian granites of Carajás Province, Amazonian Craton: The origin of hydrated granites associated with charnockites. Lithos 277, 3–32.

Donaire, T., Pascual, E., Pin, C., Duthou, J.-L., 2005. Microgranular enclaves as evidence of rapid cooling in granitoid rocks: the case of the Los Pedroches granodiorite, Iberian Massif, Spain. Contributions to Mineralogy and Petrology 149(3), 247–265.

Dostal, J., Chatterjee, A.K., 1995. Origin of Topaz-Bearing and Related Peraluminous Granites of the Late Devonian Davis Lake Pluton, Nova-Scotia, Canada - Crystal Versus Fluid Fractionation. Chemical Geology 123(1–4), 67–88.

Ferry, J.M., Watson, E.B., 2007. New thermodynamic models and revised calibrations for the Ti-in-zircon and Zr-in-rutile thermometers. Contributions to Mineralogy and Petrology 154(4), 429–437.

Foster, M.D., 1960. Interpretation of the composition of trioctahedral Mica. United States Geological Survey Professional Paper 354-E, 11–48.

Frost, B.R. et al., 2001. A geochemical classification for granitic rocks. Journal of Petrology 42, 2033–2048.

Griffin, W.L. et al., 2000. The Hf isotope composition of cratonic mantle: LAM-MC-ICPMS analysis of zircon megacrysts in kimberlites. Geochimica Et Cosmochimica Acta 64(1), 133–147.

Griffin, W.L., Pearson, N.J., Belousova, E.A., Saeed, A., 2007. Reply to "Comment to short-communication 'Comment: Hf-isotope heterogeneity in zircon 91500' by W.L. Griffin, N.J. Pearson, E.A. Belousova and A. Saeed (Chemical Geology 233 (2006) 358–363)" by F. Corfu. Chemical Geology 244(1–2), 354–356.

Griffin, W.L. et al., 2002. Zircon chemistry and magma mixing, SE China: In-situ analysis of Hf isotopes, Tonglu and Pingtan igneous complexes. Lithos 61(3–4), 237–269.

He, Z.Y., Xu, X.S., 2012. Petrogenesis of the Late Yanshanian mantle-derived intrusions in southeastern China: Response to the geodynamics of paleo-Pacific plate subduction. Chemical Geology 328, 208–221.

He, Z.Y., Xu, X.S., Niu, Y., 2010. Petrogenesis and tectonic significance of a Mesozoic granite–syenite–gabbro association from inland South China. Lithos 119(3–4), 621–641.

Hsieh, P.S., Chen, C.H., Yen, C.M., Lee, C.Y., 2009. Origin of Mafic Microgranular

Enclaves (MMEs) and Their Host Rocks of the Cretaceous Xiaojiang-Liangnong Granitic Complexes in the Southeast Coast Magmatic Belt, S China. Terrestrial, Atmospheric and Oceanic Sciences 20(3).

Irvine, T.N., Baragar, W.R.A., 1971. A guide to the chemical classification of the common volcanic rocks. Canadian Journal of Earth Sciences 8, 523–548.

Jiang, Y.H., Jia, R.Y., Liu, Z., Liao, S.Y., Zhao, P., Zhou, Q., 2013. Origin of Middle Triassic high-K calc-alkaline granitoids and their potassic microgranular enclaves from the western Kunlun orogen, northwest China: A record of the closure of Paleo-Tethys. Lithos 156–159, 13–30.

Jiang, Y.H., Wang, G.C., Liu, Z., Ni, C.Y., Qing, L., Zhang, Q., 2015. Repeated slab advance–retreat of the Palaeo-Pacific plate underneath SE China. International Geology Review 57(4), 472–491.

Jiang, Y.H., Zhao, P., Zhou, Q., Liao, S.Y., Jin, G.D., 2011. Petrogenesis and tectonic implications of Early Cretaceous S- and A-type granites in the northwest of the Gan-Hang rift, SE China. Lithos 121(1–4), 55–73.

Jiang, Y.H. et al., 2009. Middle to late Jurassic felsic and mafic magmatism in southern Hunan province, southeast China: Implications for a continental arc to rifting. Lithos 107(3–4), 185–204.

Li, B., Jiang S.Y., Lu A.H., Zhao H.X., Yang T.L., Hou M.L. 2016. Zircon U–Pb dating, geochemical and Sr–Nd–Hf isotopic characteristics of the Jintonghu monzonitic rocks in western Fujian Province, South China: Implication for

Cretaceous crust–mantle interactions and lithospheric extension. Lithos 260, 413–428.

Li, J.H, Zhang, Y.Q, Dong, S.W, Johnston, S.T., 2014a. Cretaceous tectonic evolution of South China: A preliminary synthesis. Earth-Science Reviews 134, 98–136.

Li, X.H., Li, Z.X., Li, W.X., Liu, Y., Yuan, C., Wei, G., Qi, C., 2007. U–Pb zircon, geochemical and Sr–Nd–Hf isotopic constraints on age and origin of Jurassic I- and A-type granites from central Guangdong, SE China: A major igneous event in response to foundering of a subducted flat-slab? Lithos 96(1–2), 186–204.

Li, Z.X., Li, X.H., 2007. Formation of the 1300-km-wide intracontinental orogen and postorogenic magmatic province in Mesozoic South China: A flat-slab subduction model. Geology, 35(2).

Li, Z., Qiu, J.S., Xu, X.S., 2012b. Geochronological, geochemical and Sr–Nd–Hf isotopic constraints on petrogenesis of Late Mesozoic gabbro–granite complexes on the southeast coast of Fujian, South China: insights into a depleted mantle source region and crust–mantle interactions. Geological Magazine 149(03), 459–482.

Li, Z., Qiu, J.S., Yang, X.M., 2014b. A review of the geochronology and geochemistry of Late Yanshanian (Cretaceous) plutons along the Fujian coastal area of southeastern China: Implications for magma evolution related to slab break-off and rollback in the Cretaceous. Earth-Science Reviews 128, 232–

248.

Liang, H. Y. et al., 2006. Zircon Ce4+/Ce3+ ratios and ages for Yulong ore-bearing porphyries in eastern Tibet. Mineralium Deposita 41(2), 152–159.

Lin W.W., Peng L.J., 1994. The estimation of Fe^{3+} and Fe^{2+} contents in amphibole and biotite from EMPA data. Journal of Changchun University of Earth Sciences 24(2), 155-162.

Liu, L., Qiu, J.S., Li, Z., 2013. Origin of mafic microgranular enclaves (MMEs) and their host quartz monzonites from the Muchen pluton in Zhejiang Province, Southeast China: Implications for magma mixing and crust–mantle interaction. Litho 160–161, 145–163.

Liu, L., Qiu, J.S., Zhao, J.L., 2016a. A hybrid origin for two Cretaceous monzonitic plutons in eastern Zhejiang Province, Southeast China: Geochronological, geochemical, and Sr–Nd–Hf isotopic evidence. Journal of Asian Earth Sciences 115, 183–203.

Liu, L., Qiu, J.S., Zhao, J.L., Yang, Z.L., 2014~~a~~. Geochronological, geochemical, and Sr–Nd–Hf isotopic characteristics of Cretaceous monzonitic plutons in western Zhejiang Province, Southeast China: New insights into the petrogenesis of intermediate rocks. Lithos 196–197, 242–260.

Liu, L., Xu, X., Xia, Y., 2016b. Asynchronizing paleo-Pacific slab rollback beneath SE China: Insights from the episodic Late Mesozoic volcanism. Gondwana Research 37, 397–407.

Liu, Y., Hu, Z., Zong, K., Gao, C., Gao, S., Xu, J., Chen, H., 2010. Reappraisement and refinement of zircon U-Pb isotope and trace element analyses by LA-ICP-MS. Chinese Science Bulletin 55(15), 1535–1546.

Maas, R., Nicholls, I.A., Legg, C., 1997. Igneous and metamorphic enclaves in the S-type Deddick granodiorite, Lachlan Fold Belt, SE Australia: Petrographic, geochemical and Nd-Sr isotopic evidence for crustal melting and magma mixing. Journal of Petrology 38(7), 815–841.

Maniar, P.D., Piccoli, P.M., 1989. Tectonic discrimination of granitoids. Geological Society of America Bulletin 101, 635–643.

McDonough, W.F., Sun, S.S., 1995. The composition of the Earth. Chemical Geology 120, 223–253.

Meng, L., Li, Z.X., Chen, H., Li, X.H., Wang, X.-C., 2012. Geochronological and geochemical results from Mesozoic basalts in southern South China Block support the flat-slab subduction model. Lithos 132-133, 127–140.

Middlemost, E.A.K., 1985. Magma and Magmatic Rocks. Longman, London.

Middlemost, E.A.K., 1994. Naming Materials in the Magma Igneous Rock System. Earth-Science Reviews 37(3–4), 215–224.

Miller, R.G., Onions, R.K., 1985. Source of Precambrian Chemical and Clastic Sediments. Nature 314(6009), 325–330.

Moghazi, A.M., Harbi, H.M., Ali, K.A., 2011. Geochemistry of the Late Neoproterozoic Hadb adh Dayheen ring complex, Central Arabian Shield:

Implications for the origin of rare-metal-bearing post-orogenic A-type granites. Journal of Asian Earth Sciences 42(6), 1324–1340.

Morimoto, N. et al., 1988. Nomenclature of Pyroxenes. Mineralogy and Petrology 39(1), 55–76.

Nurmi, P.A., Haapala, I., 1986. The Proterozoic granitoids of Finland: granite types, metallogeny and relation to crustal evolution. Bulletin of Geological Society of Finland 58, 431–453.

Patiño Douce, A.E., 1999. What do experiments tell us about the relative contributions of crust and mantle to the origin of granitic magmas? Geological Society, London, Special Publications 168(1), 55–75.

Pearce, J.A., Stern, R.J., Bloomer, S.H., Fryer, P., 2005. Geochemical mapping of the Mariana arc-basin system: Implications for the nature and distribution of subduction components. Geochemistry, Geophysics, Geosystems 6(7), n/a-n/a.

Peccerillo, A., Taylor, D.R., 1976. Geochemistry of Eocene calc-alkaline volcanic rocks from the Kastamonu area, Northern Turkey. Contributions to Mineralogy and Petrology 58, 63–91.

Plank, T., Kelley, K.A., Zimmer, M.M., Hauri, E.H., Wallace, P.J., 2013. Why do mafic arc magmas contain ~4wt% water on average? Earth and Planetary Science Letters 364, 168–179.

Qi, L., Hu, J., D.Conrad, G., 2000. Determination of trace elements in granites by inductively coupled plasma mass spectrometry. Talanta 51(3), 507–513.

Qi, Y., Hu, R.Z., Liu, S., Coulson, I. M., Qi, H.W., Tian, J.J, Zhu J.J., 2016. Petrogenesis and geodynamic setting of Early Cretaceous mafic–ultramafic intrusions, South China: A case study from the Gan–Hang tectonic belt. Lithos 258–259, 149–162.

Qiu, J.S., Jiang, S.Y., Hu, J., McInnes, B.I.A., Ling, H.F., 2006. Isotopic dating of the Mikengshan tin ore-field in Huichang county, Jiangxi province, and its implications to metallogenesis. Acta Petrologica Sinica 22, 2444–2450. （In Chinese with English abstract）.

Qiu, J.S., Li, Z., Liu, L., Zhao, J.L., 2012. Petrogenesis of the Zhangpu composite granite pluton in Fujian province: constraints from zircon U–Pb ages, elemental geochemistry and Nd–Hf isotopes. Acta Geologica Sinica 86, 561–576 (in Chinese with English abstract).

Ribeiro, J. M., Stern, R. J., Kelley, K. A., Martinez, F., Ishizuka, O., Manton, W. I., Ohara, Y., 2013. Nature and distribution of slab-derived fluids and mantle sources beneath the Southeast Mariana forearc rift. Geochemistry Geophysics Geosystems 14(10), 4585–4607.

Rudnick, R.L., Fountain, D.M., 1995. Nature and Composition of the Continental-Crust - a Lower Crustal Perspective. Reviews of Geophysics 33(3): 267-309.

Shen, W.Z., Zhu, J.C., Liu, C.S., Xu, S.J., Ling, H.F., 1993. Sm–Nd isotopic study of basement metamorphic rocks in south China and its constraint on material

sources of granitoids. Acta Petrologica Sinica 9, 115–124.

Smythe, D.J., Brenan, J.M., 2016. Magmatic oxygen fugacity estimated using zircon-melt partitioning of cerium. Earth and Planetary Science Letters 453, 260–266.

Sun, W., Ding, X., Hu, Y.H., Li, X.H., 2007. The golden transformation of the Cretaceous plate subduction in the west Pacific. Earth and Planetary Science Letters 262(3–4), 533–542.

Wang, D.X., Li, C.L., Gao, W.L., Wang, Z.X., Zhao, Z.D., 2013. Late Mesozoic magma mixing in eastern Zhejiang Province: Evidence from U-Pb geochronology and geochemistry of Xiaojiang pluton in Xinchang. Acta Petrologica Sinica 29, 3993–4003 (in Chinese with English abstract).

Wang, F.Y., Ling, M.X., Ding, X., Hu, Y.H., Zhou, J.B., Yang, X.Y., Liang, H.Y., Fan, W.M., Sun, W.D., 2011. Mesozoic large magmatic events and mineralization in SE China: oblique subduction of the Pacific plate. International Geology Review 53(5-6), 704–726.

Waters, L.E., Lange, R.A., 2015. An updated calibration of the plagioclase-liquid hygrometer-thermometer applicable to basalts through rhyolites. American Mineralogist 100(10), 2172–2184.

Whalen, J.B., Currie, K.L., Chappell, B.W., 1987. A-Type Granites - Geochemical Characteristics, Discrimination and Petrogenesis. Contributions to Mineralogy and Petrology 95(4), 407–419.

Wones, D.R., Eugster, H.P., 1965. Stability of biotite-experiment theory and application. American Mineralogist 50, 1228–1272.

Wong, J., Sun, M., Xing, G.F, Li, X.H., Zhao, G.C, Wong, K., Wu, F.Y, 2011. Zircon U–Pb and Hf isotopic study of Mesozoic felsic rocks from eastern Zhejiang, South China: Geochemical contrast between the Yangtze and Cathaysia blocks. Gondwana Research 19(1), 244–259.

Wong, J., Sun, M., Xing, G.F., Li, X.H., Zhao, G.C, Wong, K., Yuan, C., Xia, X.P, Li, L.M., Wu, F.Y., 2009. Geochemical and zircon U–Pb and Hf isotopic study of the Baijuhuajian metaluminous A-type granite: Extension at 125–100 Ma and its tectonic significance for South China. Lithos 112(3-4), 289-305.

Xu, X., O'Reilly, S.Y., Griffin, W. L., Wang, X.L, Pearson, N. J., He, Z.Y., 2007. The crust of Cathaysia: Age, assembly and reworking of two terranes. Precambrian Research 158(1–2), 51–78.

Yang, J.H., Wu, F.Y., Wilde, S.A., Xie, L.W., Yang, Y.H., Liu, X.M., 2007. Tracing magma mixing in granite genesis: in situ U–Pb dating and Hf-isotope analysis of zircons. Contributions to Mineralogy and Petrology 153(2), 177–190.

Yang, Y.H., Zhang, H.F., Chu, Z.Y., Xie, L.W., Wu, F.Y., 2010. Components and episodic growth of Precambrian crust in the Cathaysia Block, South China: Evidence from U–Pb ages and Hf isotopes of zircons in Neoproterozoic sediments. Precambrian Research 181(1–4), 97–114.

Yu, J.H., O'Reilly, S.Z., Wang, L.J., Griffin, W.L., Zhou, M.F., Zhang, M., Shu L.S.,

2010. Components and episodic growth of Precambrian crust in the Cathaysia Block, South China: Evidence from U–Pb ages and Hf isotopes of zircons in Neoproterozoic sediments. Precambrian Research, 181(1-4): 97–114.

Zhao, J.L., Qiu, J.S., Liu, L., Wang, R.Q., 2016. The Late Cretaceous I- and A-type granite association of southeast China: Implications for the origin and evolution of post-collisional extensional magmatism. Lithos 240, 16–33.

Zheng, Y.F., Xiao, W.J., Zhao, G., 2013. Introduction to tectonics of China. Gondwana Research 23(4), 1189–1206.

Zhou, J., Jiang, Y.H., Xing, G., Zeng, Y., Ge, W., 2013. Geochronology and petrogenesis of Cretaceous A-type granites from the NE Jiangnan Orogen, SE China. International Geology Review 55(11), 1359–1383.

Zhou, X.M., Li, W.X., 2000. Origin of Late Mesozoic igneous rocks in Southeastern China: implications for lithosphere subduction and underplating of mafic magmas. Tectonophysics 326(3–4), 269–287.

Zhou, X.M., Sun, T., Shen, W.Z., Shu, L.S., Niu, Y.L., 2006. Petrogenesis of Mesozoic granitoids and volcanic rocks in South China: A response to tectonic evolution. Episodes 29(1), 26–33.

Zhu, K.Y., Li, Z.X., Xu, X.S., Wilde, S.A., Chen, H.L., 2016. Early Mesozoic ferroan (A-type) and magnesian granitoids in eastern South China: Tracing the influence of flat-slab subduction at the western Pacific margin. Lithos 240–243, 371–381.

Fig. 1. Simplified geological map of south China showing the distribution of Mesozoic granitoid and volcanic rocks (modified after Zhou et al., 2006). Also shown are the Cretaceous syenites, monzonites and mafic rocks. Data source: Pingtan gabbro (Griffin et al., 2002), Mikengshan granite (Qiu et al., 2006), Suzhou and Baijuhuajian granites (Wong et al., 2009), Tongshan granite (Jiang et al., 2011), Changqiao granite (Qiu et al., 2012), Quanzhou and Huacuo gabbro (Li et al., 2012~~b~~), Fuzhou, Daheshan, Honggong, Caiyuan and Huantuling syenites (He and Xu, 2012), Muchen monzonite (Liu et al., 2013); Fuling and Lingshan granites (Zhou et al., 2013), Matou and Dalai monzonites (Liu et al., 2014), Huangtanyang and Kanggu monzonites (Liu et al., 2016a), Jintonghu monzonite (Li et al., 2016), Quzhou and Longyou mafic rocks (Qi et al., 2016).

Fig. 2. (a) Simplified map of China; (b) Simplified geological map of Zhejiang Province showing the distribution of Mesozoic granitoid (modified after Zhou et al., 2006); (c) Simplified geological map of the Xiaojiang and Beizhang plutons (modified after the Geological Maps of Ningbo Sheet 1:200,000).

Fig. 3. Macroscopic images showing the host granitoids, MMEs and dolerite dyke from Xiaojiang and Beizhang plutons. (a) Alkali feldspar granite intruded by quartz diorite from Xiaojiang Pluton; (b) alkali feldspar granite and its MME from Xiaojiang Pluton; (c) and (d) quartz diorites and their MMEs from Xiaojiang Pluton; (e) MMEs

with an irregular shape in the monzogranite from Beizhang pluton; (f) dolerite dyke intruding into the monzogranite from Beizhang pluton.

Fig. 4. Thin section photographs of rocks from Xiaojiang and Beizhang plutons. (a) Alkali feldspar granite; (b) quartz diorite; (c) monzogranite; (d) MME from alkali feldspar granite; (e) and (f) MME from quartz diorite; (g) MME from monzogranite; (h) dolerite. All the thin section photographs were taken using a Laika microscope under cross-polarised light (Qtz = quartz, Af = alkali-feldspar, Pl = plagioclase, Bi = biotite, Cpx = clinopyroxene, Opx = orthopyroxene).

Fig. 5. Representative cathodoluminescence (CL) images of selected zircons from the Xiaojiang and Beizhang plutons. The morphology of zircon grains, $^{206}Pb/^{238}U$ ages, and $\varepsilon_{Hf}(t)$ values are shown. Small circles (with solid lines) indicate the U–Pb dating positions, and large circles (with dashed lines) indicate the sites of Hf isotope analyses, with circle diameters showing the approximate laser spot sizes.

Fig. 6. LA-ICP-MS zircon U–Pb concordia diagrams (a-g) and chondrite-normalized REE patterns of zircons (g; normalisation values from McDonough and Sun, 1995) for the Xiaojiang and Beizhang plutons.

Fig. 7. (a) Classification diagram for biotites from the Xiaojiang and Beizhang

plutons (modified after Foster, 1960); (b) Diagram of Fe^{3+}–Fe^{2+}–Mg for biotite from Xiaojiang and Beizhang plutons (modified after Wones and Eugster (1965), Fe^{2+} and Fe^{3+} are corrected according to Lin and Peng (1994)). (HM, hematite-magnetite; NNO, Nickel-nickel oxide; FMQ, fayalite-magnetite-quartz); (c) Classification diagram for feldspars from the Xiaojiang and Beizhang plutons; (d) Classification diagram for pyroxenes from the Xiaojiang and Beizhang plutons (modified after Morimoto et al., 1988).

Fig. 8. Chemical classification of rocks from the Xiaojiang and Beizhang plutons. (a) Total alkali vs. silica (TAS) diagram (Middlemost, 1994); with the thick solid line from Irvine and Baragar (1971); (b) $FeO^T/(FeO^T+MgO)$ versus SiO_2 plot with ferroan-magnesian granitoid classification (Frost et al., 2001); (c) K_2O vs. SiO_2 diagram (solid lines from Peccerillo and Taylor (1976) and dashed lines from Middlemost (1985)); (d) A/NK vs. A/CNK diagram (Chappell and White, 1974; Maniar and Piccoli, 1989).

Fig. 9. Chondrite-normalized REE (a and c; normalisation values from Boynton (1984) and primitive-mantle-normalized multi-element patterns (b and d; normalisation values from McDonough and Sun (1995) for rocks from the Xiaojiang and Beizhang plutons.

Fig. 10. (a) $\varepsilon_{Nd}(t)$ vs. age diagram for samples from the Xiaojiang and Beizhang plutons. DM, depleted mantle; CHUR, chondritic uniform reservoir. Line A represents the Proterozoic crustal end-member with higher degree of maturation in the SCB, with average isotopic compositions of $^{147}Sm/^{144}Nd = 0.1198$ and $^{143}Nd/^{144}Nd = 0.511822$; line B represents the Proterozoic crustal end-member with lower degree of maturation in the SCB, with average isotopic compositions of $^{147}Sm/^{144}Nd = 0.1246$ and $^{143}Nd/^{144}Nd = 0.512170$ (Shen et al., 1993). (b) $\varepsilon_{Hf}(t)$ vs. age diagram for zircons from the Xiaojiang and Beizhang plutons. The values used for constructing the depleted mantle (DM) and crustal evolution reference lines were taken from Griffin et al. (2000) and Griffin et al. (2002). The Hf evolutionary area shown for the crustal basement of the Cathaysia Block is from Xu et al. (2007).

Fig. 11. (a) $Al_2O_3/(FeO^T+MgO+TiO_2)$ vs. $Al_2O_3+FeO^T+MgO+TiO_2$ diagram (modified after Patiño Douce, 1999). (b) molar K_2O/Na_2O vs. molar $CaO/(MgO+FeO^T)$ diagram (modified after Altherr and Siebel, 2002). (c) Th/Nb vs. Ba/Th diagram with sediment melt and aqueous fluids trends from (Ribeiro et al., 2013). (d) Th/Yb vs. Sr/Nd diagram. (e) Mg# vs. SiO_2 diagram for the Huangtanyang and Kanggu plutons (Jiang et al., 2013 and references therein); (f) $\varepsilon_{Nd}(t)$ vs. La/Nb diagram for the Huangtanyang and Kanggu plutons. The OIB-asthenosphere and South China subcontinental lithosphere are after Chen et al. (2008). The values for the Cretaceous basaltic rocks in the coastal region of Cathaysia Block are from Meng et al.

(2012).

Fig. 12. logfO_2 vs. Temperature (°C) diagram (a and b; modified after (Smythe and Brenan, 2016). Average error in calculated logfO_2 is shown in the upper left corner, temperatures were calculated using zircon Ti contents and the calibration of Ferry and Watson (2007). (HM, hematite-magnetite; NNO, Nickel-nickel oxide; FMQ, fayalite-magnetite-quartz; WM, wustite-magnetite; IW, iron- wüstite; QIF, quartz-iron-fayalite).

Fig. 13. Age vs. Ba/Nb and La/Nb plots for the representative Cretaceous rocks of Southeast China

Data source: Suzhou granite (Charoy and Raimbault, 1994), Pingtan gabbro (Griffin et al., 2002), Mikengshan granite (Qiu et al., 2006), Baijuhuajian granite (Wong et al., 2009), Tongshan granite (Jiang et al., 2011), Changqiao granite (Qiu et al., 2012), Quanzhou and Huacuo gabbro (Li et al., 2012), Fuzhou, Daheshan, Honggong, Caiyuan and Huantuling syenites (He and Xu, 2012), Muchen monzonite (Liu et al., 2013), Fuling and Lingshan granites (Zhou et al., 2013), Matou and Dalai monzonites (Liu et al., 2014), Huangtanyang and Kanggu monzonites (Liu et al., 2016a), Jintonghu monzonite (Li et al., 2016), Quzhou and Longyou mafic rocks (Qi et al., 2016).

Table 1. Rb–Sr and Sm–Nd isotopic data for the Xiaojiang and Beizhang plutons

Notes: εNd(t) values are calculated by granitoid ages and based on ^{147}Sm decay constant of 6.54×10^{-12}, the ^{143}Nd/^{144}Nd and ^{147}Sm/^{144}Nd ratios of chondrite and depleted mantle at present day are 0.512630 and 0.1960, 0.513151 and 0.2136, respectively (Bouvier et al., 2008; Miller and Onions, 1985).

Table 1. Rb–Sr and Sm–Nd isotopic data for the Xiaojiang and Beizhang plutons

Sample no.	t(Ma)	Rb ($\times10^{-6}$)	Sr ($\times10^{-6}$)	^{87}Rb/^{86}Sr	^{87}Sr/^{86}Sr	I_{Sr}	^{147}Sm/^{144}Nd	^{143}Nd/^{144}Nd	$\varepsilon_{Nd}(t)$	T_{DM2} (Ga)
Alkali feldspar granite										
XJ-10	120	204	30	-	-	-	0.135	0.512326±3	-4.99	1.33
Enclave from alkali feldspar granite										
XJ-13	119.6	248	211	3.402	0.714137±7	0.708354	0.150	0.512344±4	-4.88	1.32
Quartz diorites										
XJ-2	110.5	71	908	0.226	0.708160±7	0.707804	0.103	0.512291±3	-5.30	1.35
XJ-5	109.3	76	884	0.249	0.708283±8	0.707897	0.108	0.512286±4	-5.48	1.37
Enclave from quartz diorite										
XJ-4	109.5	74	812	0.264	0.708317±6	0.707907	0.107	0.512280±4	-5.59	1.37
Monzogranite										
BZ-1	109.3	134	372	1.042	0.709589±8	0.707970	0.091	0.512260±3	-5.75	1.39
Dolerite										
BZ-5	110.2	56	912	0.178	0.708179±7	0.707901	0.102	0.512332±4	-4.50	1.29

Notes: $\varepsilon_{Nd}(t)$ values are calculated by granitoid ages and based on ^{147}Sm decay constant of 6.54×10^{-12}, the ^{143}Nd/^{144}Nd and ^{147}Sm/^{144}Nd ratios of chondrite and depleted mantle at present day are 0.512630 and 0.1960, 0.513151 and 0.2136, respectively (Bouvier et al., 2008; Miller and Onions, 1985).

Graphical abstract

Highlights

- Two episodes of mafic magmas were involved in granitoid genesis.
- Iron-enrichment in granitoid was controlled mainly by oxygen fugacity and pressure.
- The direction of motion of the paleo-Pacific plate changed in the Cretaceous.

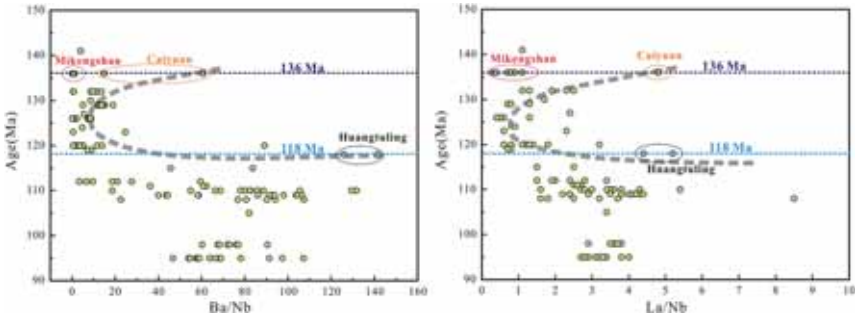

Graphics Abstract

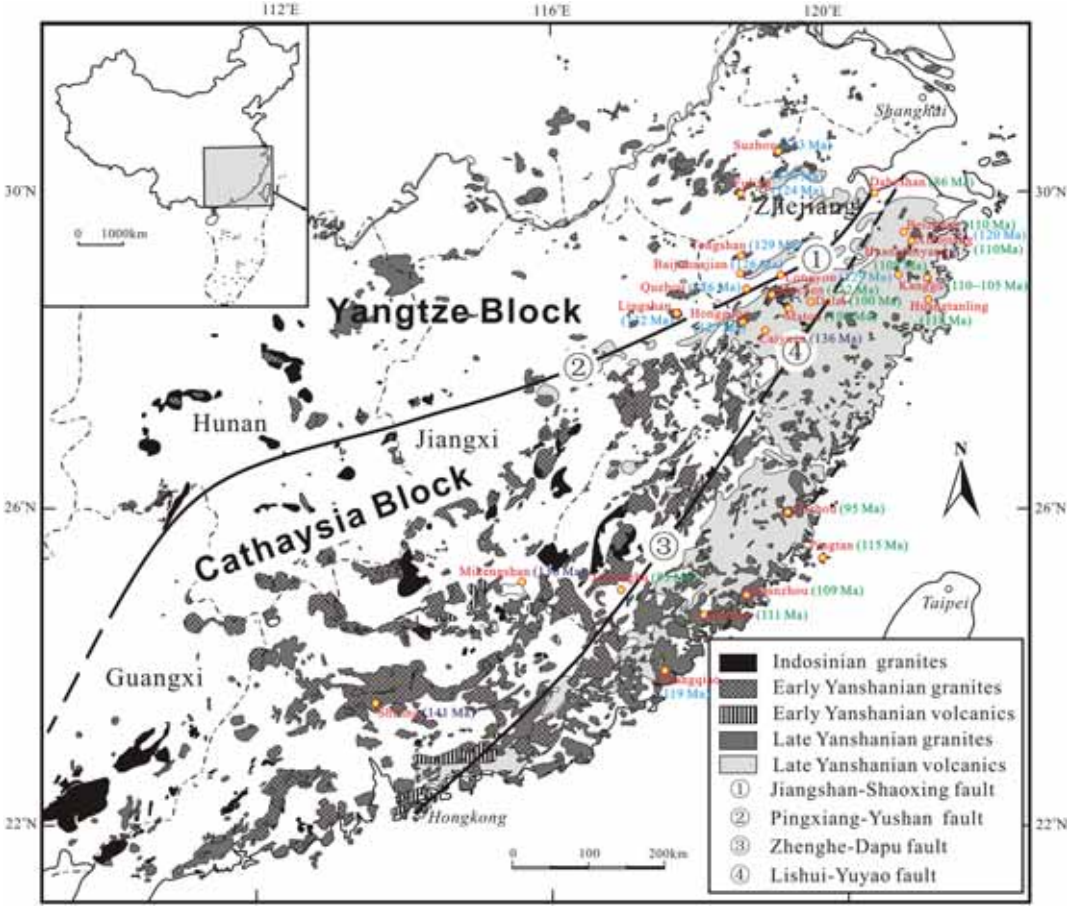
112°E
116°E
120°E
30°N
26°N
22°N
0 1000km
Yangtze Block
Cathaysia Block
Hunan
Jiangxi
Guangxi
Zhejiang
Shanghai
Taipei
Hongkong
N
0 100 200km
① Jiangshan-Shaoxing fault
② Pingxiang-Yushan fault
③ Zhenghe-Dapu fault
④ Lishui-Yuyao fault
Indosinian granites
Early Yanshanian granites
Early Yanshanian volcanics
Late Yanshanian granites
Late Yanshanian volcanics

Figure 1

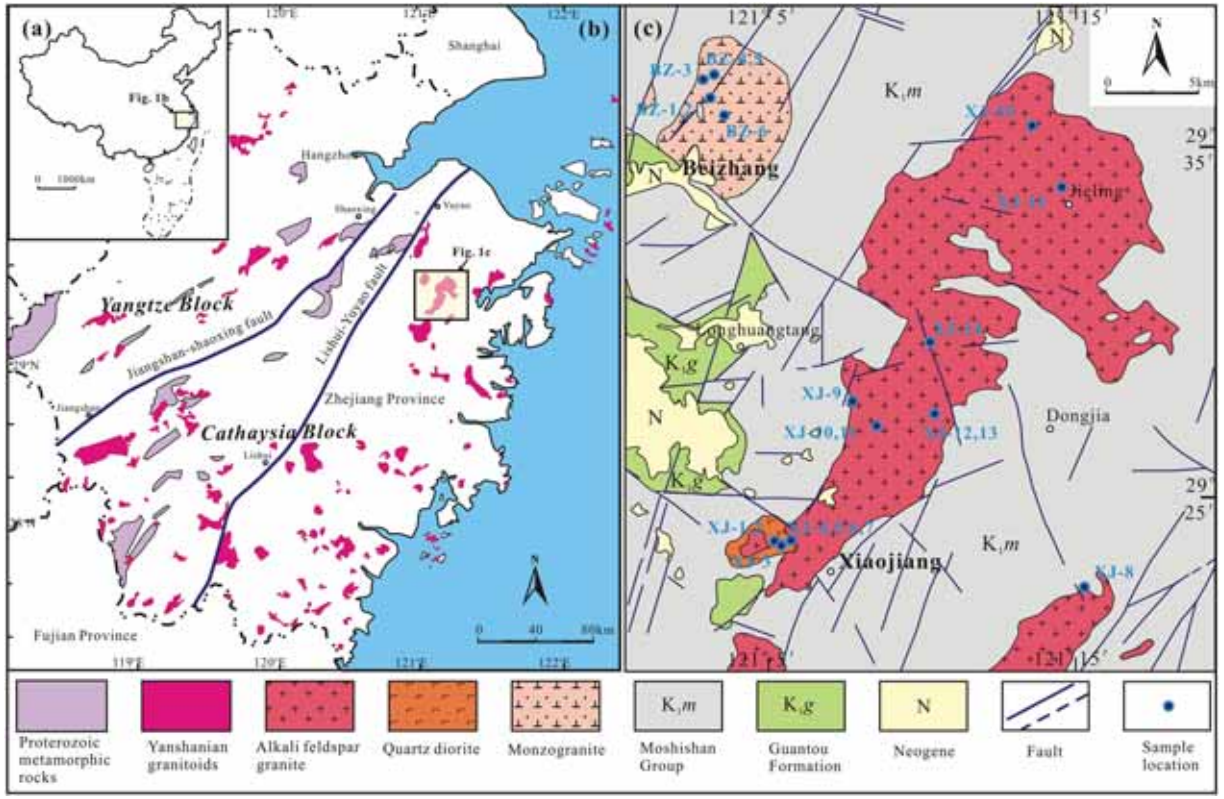
(a)
Fig. 1b
(b)
Shanghai
Hangzhou
Yueqing
Fig. 1c
Yangtze Block
Jiangshan-shaoxing fault
Lishui-Yuyao fault
Zhejiang Province
Cathaysia Block
Fujian Province
(c)
Beizhang
Jiqing
Donghuangtang
Dongjia
Xiaojiang
Proterozoic metamorphic rocks
Yanshanian granitoids
Alkali feldspar granite
Quartz diorite
Monzogranite
Moshishan Group
Guantou Formation
Neogene
Fault
Sample location

Figure 2


(a)
Alkali feldspar granite
Quartz diorite
(b)
Alkali feldspar granite
MME
(c)
MME
Quartz diorite
(d)
MME
Quartz diorite
(e)
Monzogranite
MME
(f)
Dolerite dyke
Monzogranite

Figure 3

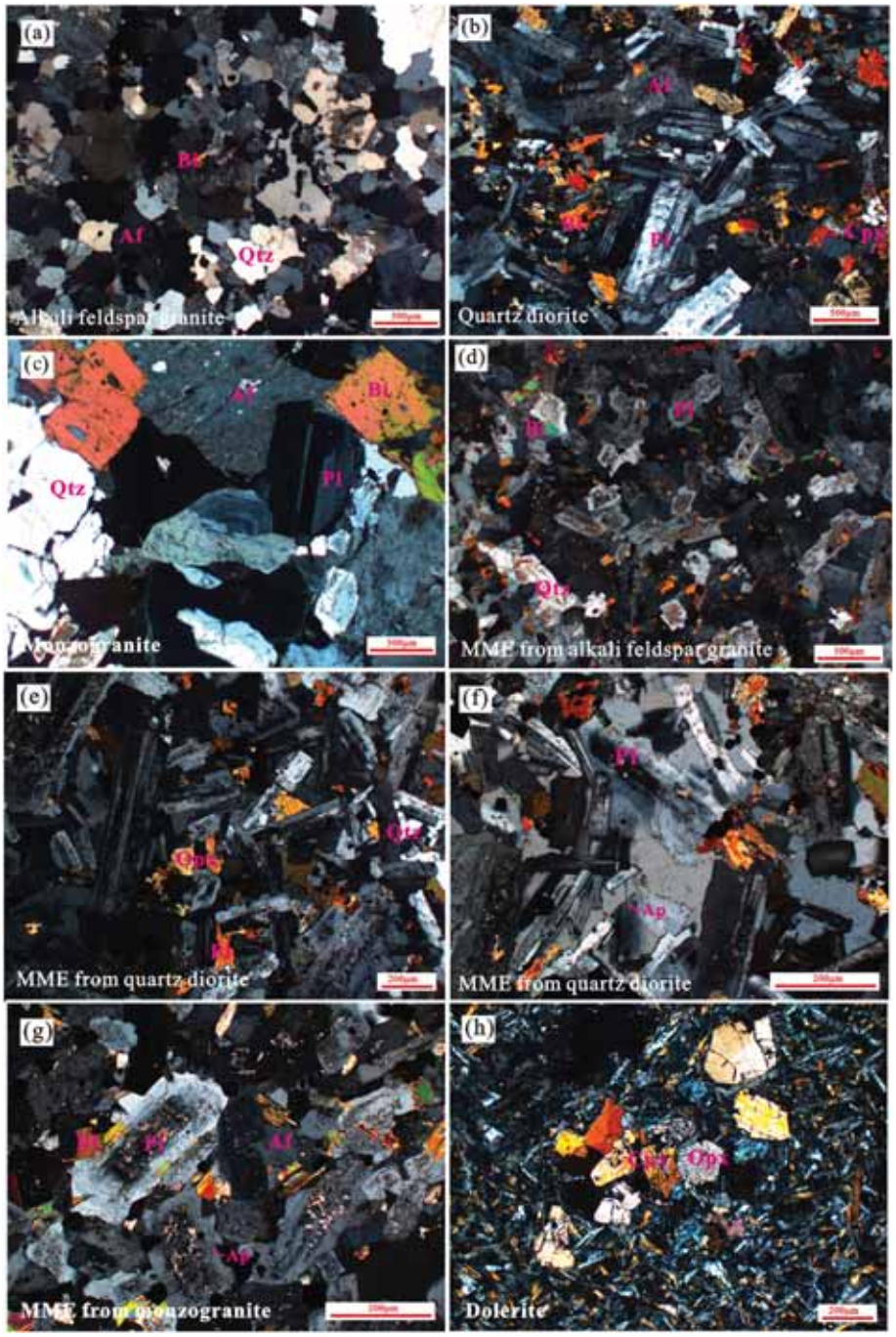
(a)
Bt
Af
Qtz
Alkali feldspar granite
(b)
Af
Bt
Pl
Cpx
Quartz diorite
(c)
Af
Bt
Qtz
Pl
Monzogranite
(d)
Pl
Bt
Qtz
MME from alkali feldspar granite
(e)
Qtz
Opx
Bt
MME from quartz diorite
(f)
Pl
Ap
MME from quartz diorite
(g)
Bt
Pl
Af
Ap
MME from monzogranite
(h)
Opx
Dolerite

Figure 4

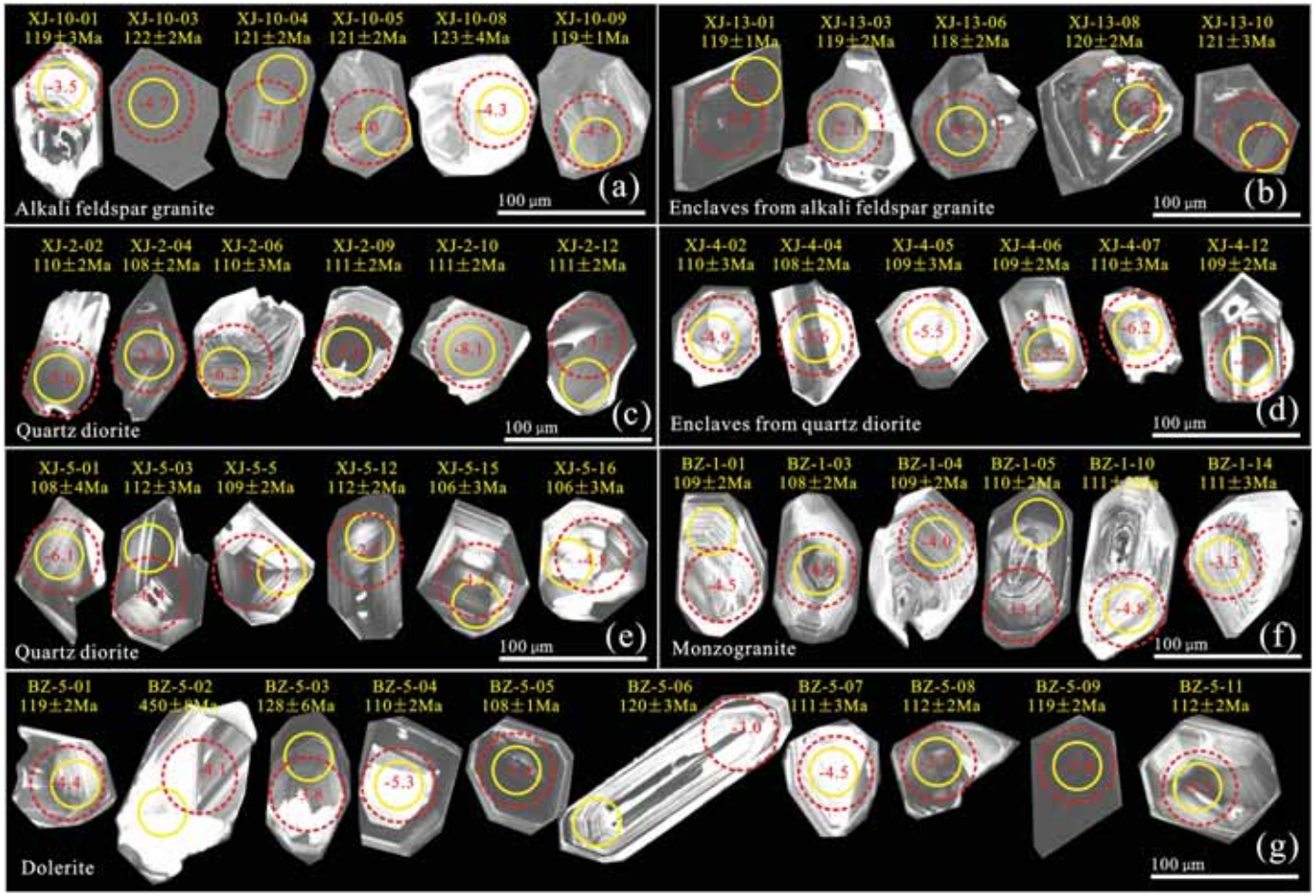
XJ-10-01 119±3Ma
XJ-10-03 122±2Ma
XJ-10-04 121±2Ma
XJ-10-05 121±2Ma
XJ-10-08 123±4Ma
XJ-10-09 119±1Ma
Alkali feldspar granite
100 μm
(a)
XJ-13-01 119±1Ma
XJ-13-03 119±2Ma
XJ-13-06 118±2Ma
XJ-13-08 120±2Ma
XJ-13-10 121±3Ma
Enclaves from alkali feldspar granite
100 μm
(b)
XJ-2-02 110±2Ma
XJ-2-04 108±2Ma
XJ-2-06 110±3Ma
XJ-2-09 111±2Ma
XJ-2-10 111±2Ma
XJ-2-12 111±2Ma
Quartz diorite
100 μm
(c)
XJ-4-02 110±3Ma
XJ-4-04 108±2Ma
XJ-4-05 109±3Ma
XJ-4-06 109±2Ma
XJ-4-07 110±3Ma
XJ-4-12 109±2Ma
Enclaves from quartz diorite
100 μm
(d)
XJ-5-01 108±4Ma
XJ-5-03 112±3Ma
XJ-5-5 109±2Ma
XJ-5-12 112±2Ma
XJ-5-15 106±3Ma
XJ-5-16 106±3Ma
Quartz diorite
100 μm
(e)
BZ-1-01 109±2Ma
BZ-1-03 108±2Ma
BZ-1-04 109±2Ma
BZ-1-05 110±2Ma
BZ-1-10
BZ-1-14 111±3Ma
Monzogranite
100 μm
(f)
BZ-5-01 119±2Ma
BZ-5-02
BZ-5-03 128±6Ma
BZ-5-04 110±2Ma
BZ-5-05 108±1Ma
BZ-5-06 120±3Ma
BZ-5-07 111±3Ma
BZ-5-08 112±2Ma
BZ-5-09 119±2Ma
BZ-5-11 112±2Ma
Dolerite
100 μm
(g)

Figure 5

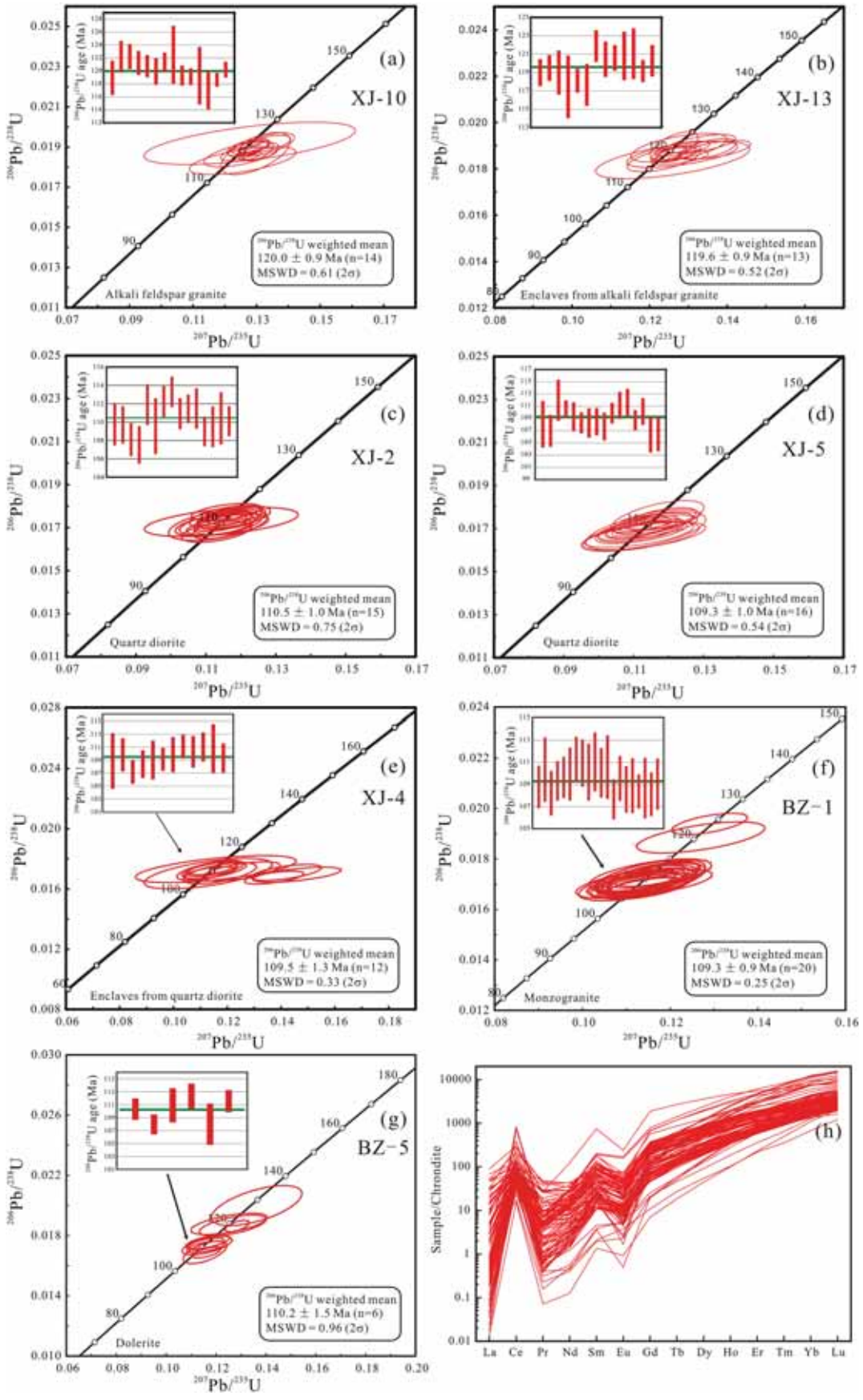
(a)
XJ-10
$^{206}Pb/^{238}U$ weighted mean
120.0 ± 0.9 Ma (n=14)
MSWD = 0.61 (2σ)
Alkali feldspar granite
(b)
XJ-13
$^{206}Pb/^{238}U$ weighted mean
119.6 ± 0.9 Ma (n=13)
MSWD = 0.52 (2σ)
Enclaves from alkali feldspar granite
(c)
XJ-2
$^{206}Pb/^{238}U$ weighted mean
110.5 ± 1.0 Ma (n=15)
MSWD = 0.75 (2σ)
Quartz diorite
(d)
XJ-5
$^{206}Pb/^{238}U$ weighted mean
109.3 ± 1.0 Ma (n=16)
MSWD = 0.54 (2σ)
Quartz diorite
(e)
XJ-4
$^{206}Pb/^{238}U$ weighted mean
109.5 ± 1.3 Ma (n=12)
MSWD = 0.33 (2σ)
Enclaves from quartz diorite
(f)
BZ-1
$^{206}Pb/^{238}U$ weighted mean
109.3 ± 0.9 Ma (n=20)
MSWD = 0.25 (2σ)
Monzogranite
(g)
BZ-5
$^{206}Pb/^{238}U$ weighted mean
110.2 ± 1.5 Ma (n=6)
MSWD = 0.96 (2σ)
Dolerite
(h)
Sample/Chrondite
La Ce Pr Nd Sm Eu Gd Tb Dy Ho Er Tm Yb Lu
$^{207}Pb/^{235}U$
$^{206}Pb/^{238}U$
$^{206}Pb/^{238}U$ age (Ma)

Figure 6

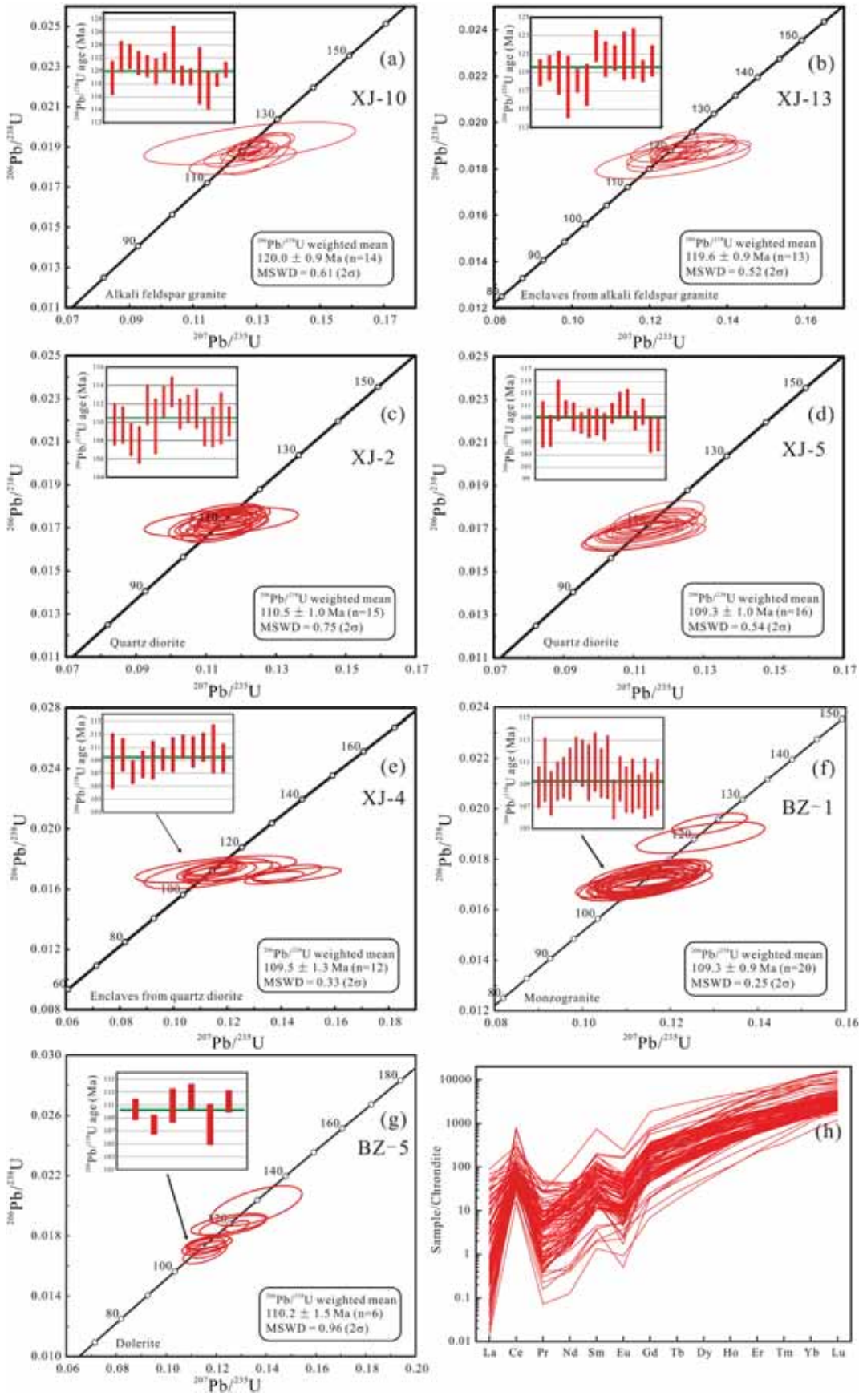
(a)
XJ-10
Alkali feldspar granite
$^{206}Pb/^{238}U$ weighted mean
120.0 ± 0.9 Ma (n=14)
MSWD = 0.61 (2σ)
(b)
XJ-13
Enclaves from alkali feldspar granite
$^{206}Pb/^{238}U$ weighted mean
119.6 ± 0.9 Ma (n=13)
MSWD = 0.52 (2σ)
(c)
XJ-2
Quartz diorite
$^{206}Pb/^{238}U$ weighted mean
110.5 ± 1.0 Ma (n=15)
MSWD = 0.75 (2σ)
(d)
XJ-5
Quartz diorite
$^{206}Pb/^{238}U$ weighted mean
109.3 ± 1.0 Ma (n=16)
MSWD = 0.54 (2σ)
(e)
XJ-4
Enclaves from quartz diorite
$^{206}Pb/^{238}U$ weighted mean
109.5 ± 1.3 Ma (n=12)
MSWD = 0.33 (2σ)
(f)
BZ-1
Monzogranite
$^{206}Pb/^{238}U$ weighted mean
109.3 ± 0.9 Ma (n=20)
MSWD = 0.25 (2σ)
(g)
BZ-5
Dolerite
$^{206}Pb/^{238}U$ weighted mean
110.2 ± 1.5 Ma (n=6)
MSWD = 0.96 (2σ)
(h)
Sample/Chrondrite
La Ce Pr Nd Sm Eu Gd Tb Dy Ho Er Tm Yb Lu
$^{206}Pb/^{238}U$
$^{207}Pb/^{235}U$

Figure 7

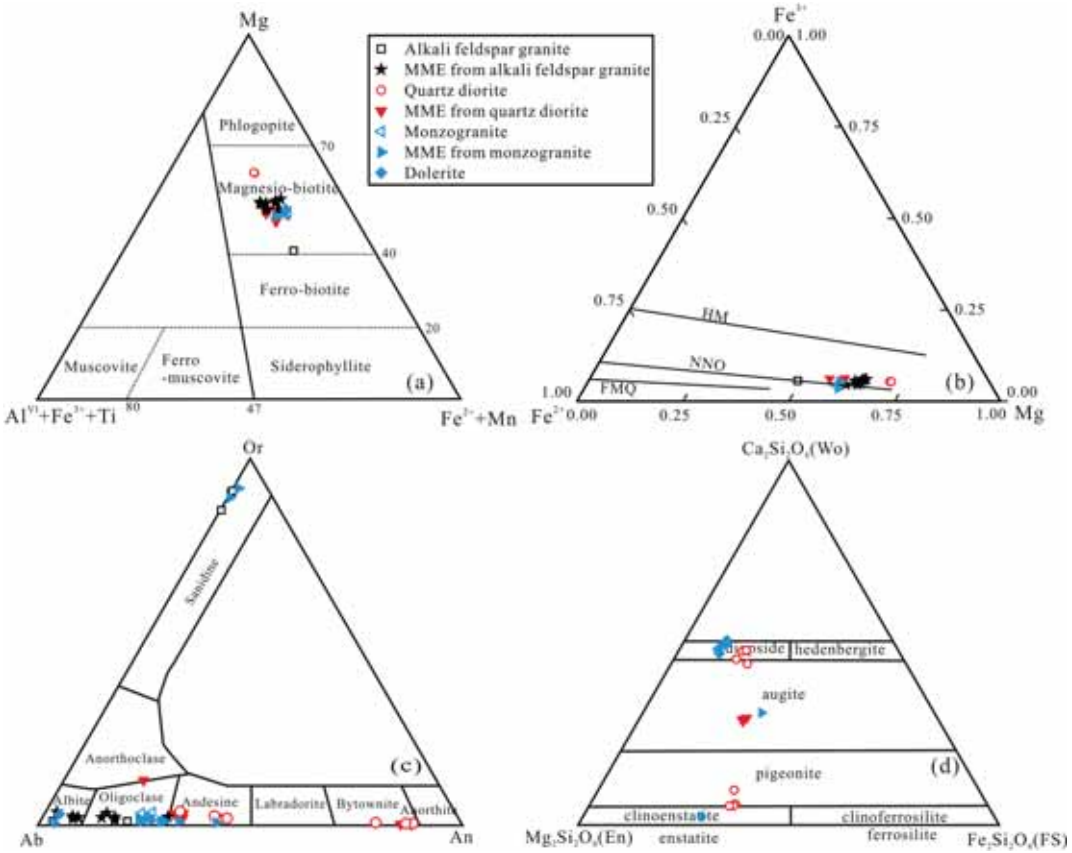
Mg
Phlogopite
Magnesio-biotite
Ferro-biotite
Muscovite
Ferro
-muscovite
Siderophyllite
(a)
70
40
20
80
47
Al^VI+Fe3++Ti
Fe3++Mn
Alkali feldspar granite
MME from alkali feldspar granite
Quartz diorite
MME from quartz diorite
Monzogranite
MME from monzogranite
Dolerite
Fe3+
0.00
1.00
0.25
0.75
0.50
0.50
0.75
0.25
HM
NNO
FMQ
(b)
1.00
0.00
Fe2+
0.00
0.25
0.50
0.75
1.00
Mg
Or
Sanidine
Anorthoclase
Albite
Oligoclase
Andesine
Labradorite
Bytownite
Anorthite
(c)
Ab
An
Ca2Si2O6(Wo)
diopside
hedenbergite
augite
pigeonite
(d)
clinoenstatite
clinoferrosilite
Mg2Si2O6(En)
enstatite
ferrosilite
Fe2Si2O6(FS)

Figure 8

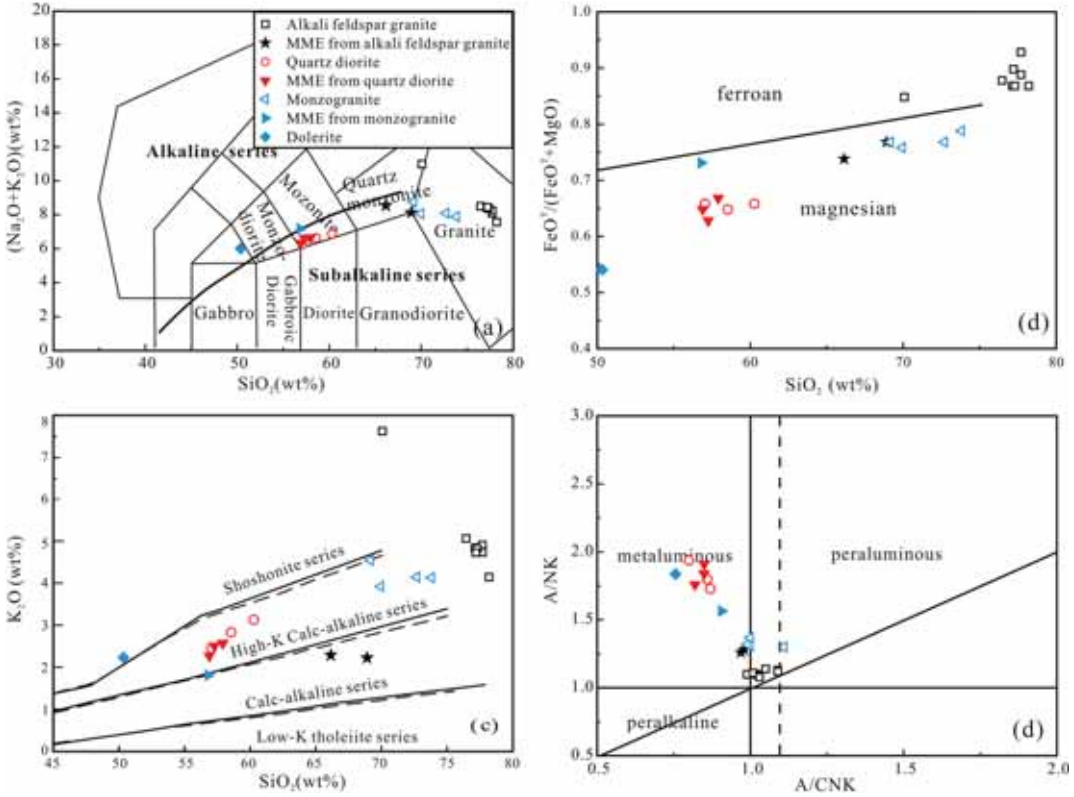
Alkali feldspar granite
MME from alkali feldspar granite
Quartz diorite
MME from quartz diorite
Monzogranite
MME from monzogranite
Dolerite
Alkaline series
Subalkaline series
Gabbro
Diorite
Granodiorite
Granite
(a)
SiO2(wt%)
(Na2O+K2O)(wt%)
ferroan
magnesian
(d)
SiO2 (wt%)
FeOt/(FeOt+MgO)
Shoshonite series
High-K Calc-alkaline series
Calc-alkaline series
Low-K tholeiite series
(c)
K2O (wt%)
metaluminous
peraluminous
peralkaline
A/NK
A/CNK

Figure 9

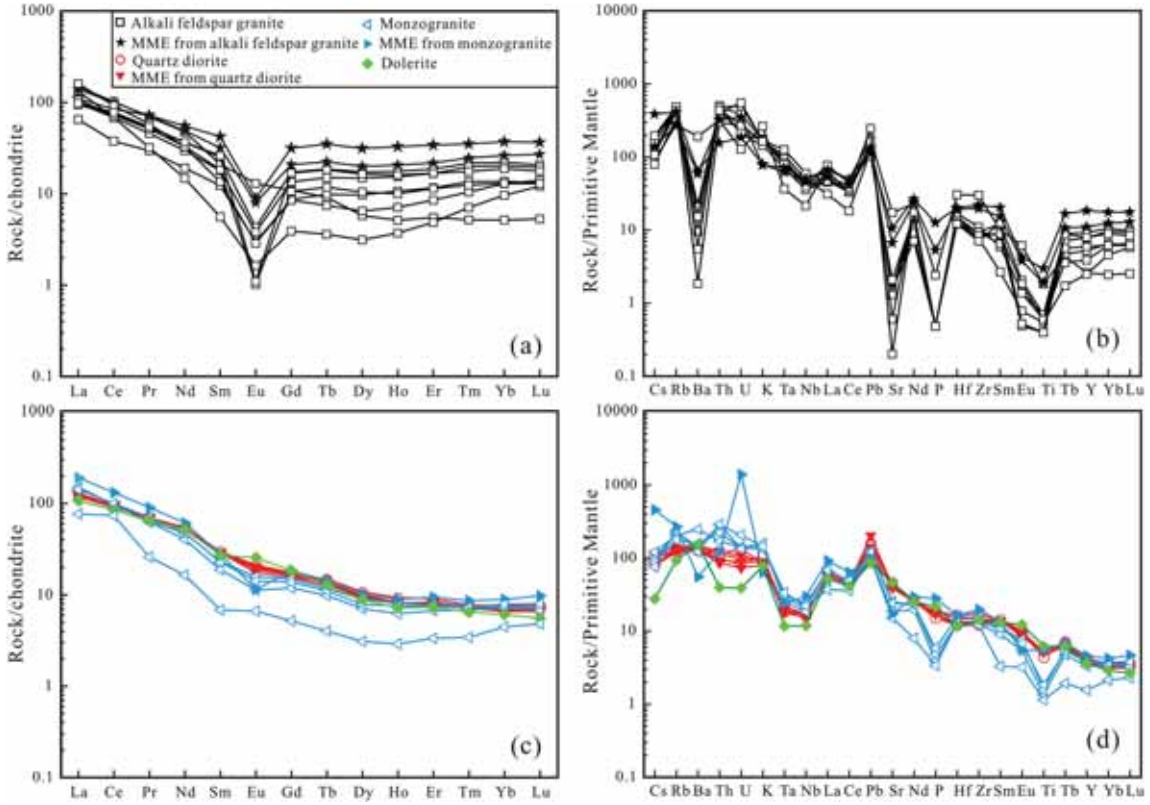
Alkali feldspar granite
MME from alkali feldspar granite
Quartz diorite
MME from quartz diorite
Monzogranite
MME from monzogranite
Dolerite
Rock/chondrite
Rock/Primitive Mantle
(a)
(b)
(c)
(d)
La Ce Pr Nd Sm Eu Gd Tb Dy Ho Er Tm Yb Lu
Cs Rb Ba Th U K Ta Nb La Ce Pb Sr Nd P Hf Zr Sm Eu Ti Tb Y Yb Lu

Figure 10

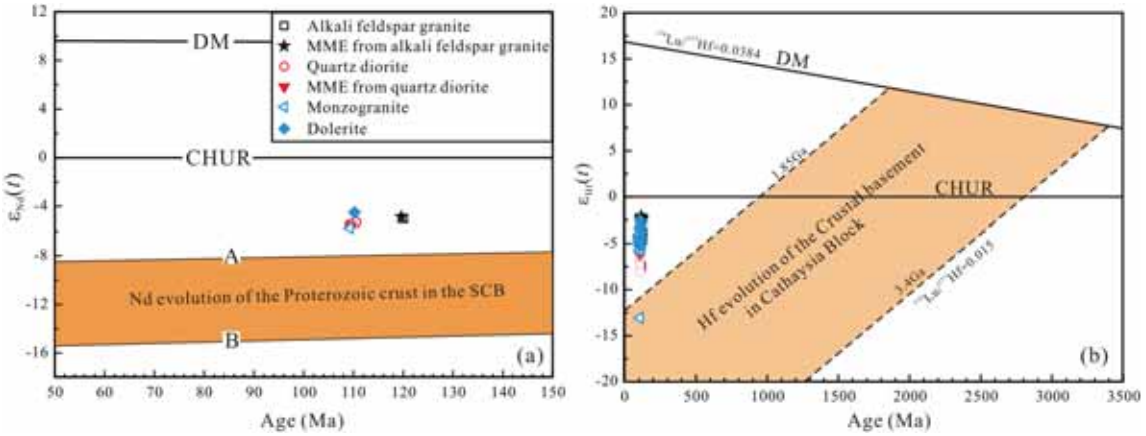
Alkali feldspar granite
MME from alkali feldspar granite
Quartz diorite
MME from quartz diorite
Monzogranite
Dolerite
DM
CHUR
A
B
Nd evolution of the Proterozoic crust in the SCB
(a)
Age (Ma)
DM
CHUR
1.55Ga
3.4Ga
Hf evolution of the Crustal basement in Cathaysia Block
(b)
Age (Ma)

Figure 11

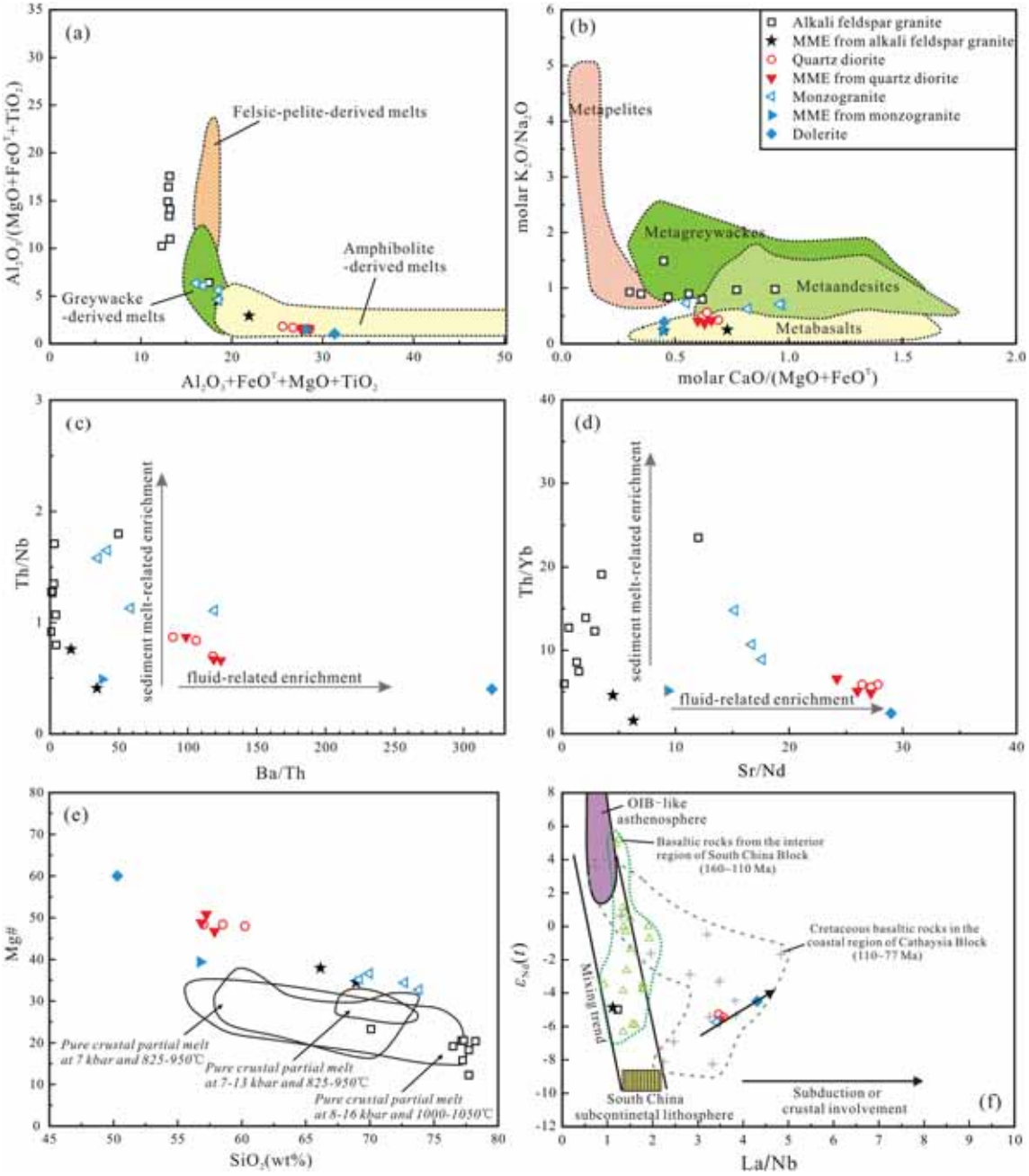
(a)
Felsic-pelite-derived melts
Amphibolite -derived melts
Greywacke -derived melts
Al2O3/(MgO+FeOT+TiO2)
Al2O3+FeOT+MgO+TiO2
(b)
Alkali feldspar granite
MME from alkali feldspar granite
Quartz diorite
MME from quartz diorite
Monzogranite
MME from monzogranite
Dolerite
Metapelites
Metagreywackes
Metaandesites
Metabasalts
molar K2O/Na2O
molar CaO/(MgO+FeOT)
(c)
sediment melt-related enrichment
fluid-related enrichment
Th/Nb
Ba/Th
(d)
sediment melt-related enrichment
fluid-related enrichment
Th/Yb
Sr/Nd
(e)
Pure crustal partial melt at 7 kbar and 825-950℃
Pure crustal partial melt at 7-13 kbar and 825-950℃
Pure crustal partial melt at 8-16 kbar and 1000-1050℃
Mg#
SiO2(wt%)
(f)
OIB-like asthenosphere
Basaltic rocks from the interior region of South China Block (160–110 Ma)
Cretaceous basaltic rocks in the coastal region of Cathaysia Block (110–77 Ma)
Mixing trend
South China subcontinetal lithosphere
Subduction or crustal involvement
εNd(t)
La/Nb

Figure 12

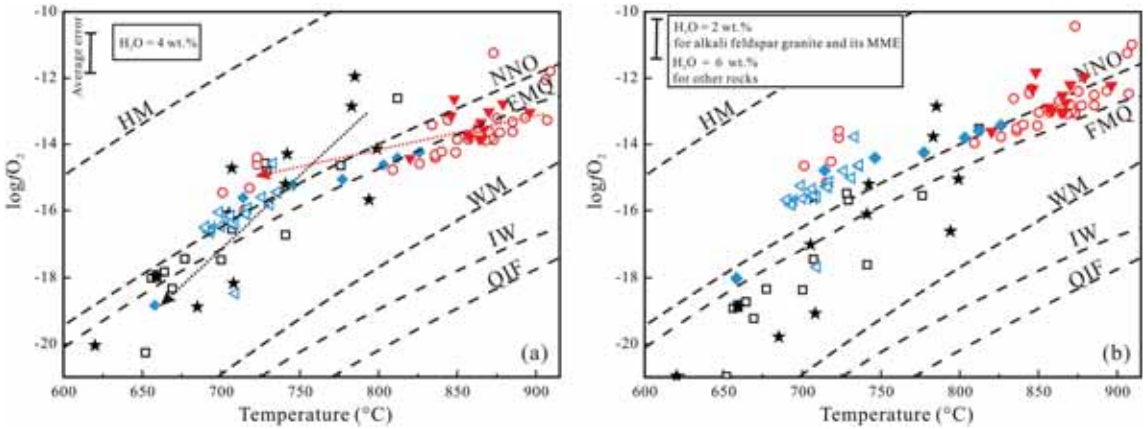
H2O = 4 wt.%
Average error
HM
NNO
FMQ
WM
IW
QIF
(a)
log/O2
Temperature (°C)
H2O = 2 wt.%
for alkali feldspar granite and its MME
H2O = 6 wt.%
for other rocks
(b)

Figure 13

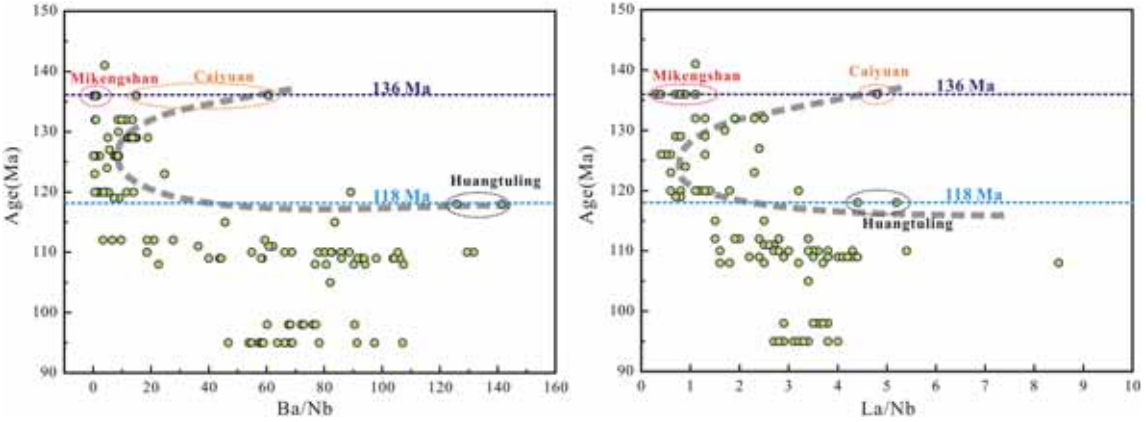
Mikengshan
Caiyuan
136 Ma
118 Ma
Huangtuling
Age(Ma)
Ba/Nb
La/Nb

Figure 14